

1 **Coupling a three-dimensional subsurface flow and transport**  
2 **model with a land surface model to simulate stream-aquifer-**  
3 **land interactions (CP v1.0)**

4

5 Gautam Bisht<sup>1</sup>, Maoyi Huang<sup>2,\*</sup>, Tian Zhou<sup>2</sup>, Xingyuan Chen<sup>2</sup>, Heng Dai<sup>2</sup>, Glenn Hammond<sup>3</sup>,  
6 William Riley<sup>1</sup>, Janelle Downs<sup>2</sup>, Ying Liu<sup>2</sup>, John Zachara<sup>2</sup>

7

8 <sup>1</sup>Lawrence Berkeley National Laboratory, Berkeley, CA

9 <sup>2</sup>Pacific Northwest National Laboratory, Richland, WA

10 <sup>3</sup>Sandia National Laboratories, Albuquerque, NM

11

12

13 Correspondence to: Maoyi Huang (maoyi.huang@pnnl.gov)

14

15

16 Revised Manuscript to be considered for *Geoscientific Model Development*

17

18 **Abstract**

19 A fully coupled three-dimensional surface and subsurface land model is developed and applied  
20 to a site along the Columbia River to simulate three-way interactions among river water,  
21 groundwater, and land surface processes. The model features the coupling of the Community  
22 Land Model version 4.5 (CLM4.5) and a massively-parallel multi-physics reactive transport  
23 model (PFLOTRAN). The coupled model, named CP v1.0, is applied to a 400 m × 400 m study  
24 domain instrumented with groundwater monitoring wells along the Columbia River shoreline.  
25 CP v1.0 simulations are performed at three spatial resolutions (i.e., 2 m, 10 m, and 20 m) over a  
26 five-year period to evaluate the impact of hydro-climatic conditions and spatial resolution on  
27 simulated variables. Results show that the coupled model is capable of simulating groundwater-  
28 river water interactions driven by river stage variability along managed river reaches, which are  
29 of global significance as a result of over 30,000 dams constructed worldwide during the past half  
30 century. Our numerical experiments suggest that the land-surface energy partitioning is strongly  
31 modulated by groundwater-river water interactions through expanding the periodically inundated  
32 fraction of the riparian zone, and enhancing moisture availability in the vadose zone via capillary  
33 rise in response to the river stage change. Furthermore, spatial resolution is found to impact  
34 significantly the accuracy of estimated the mass exchange rates at the boundaries of the aquifer,  
35 and it becomes critical when surface and subsurface become more tightly coupled with  
36 groundwater table within six to seven meters below the surface. Inclusion of lateral subsurface  
37 flow influenced both the surface energy budget and subsurface transport processes as a result of  
38 river water intrusion into the subsurface in response to elevated river stage that increased soil  
39 moisture for evapotranspiration and suppressed available energy for sensible heat in the warm  
40 season. The coupled model developed in this study can be used for improving mechanistic  
41 understanding of ecosystem functioning and biogeochemical cycling along river corridors under  
42 historical and future hydro-climatic changes. The dataset presented in this study can also serve as  
43 a good benchmarking case for testing other integrated models.

44

## 45 **1 Introduction**

46 Previous modeling studies have demonstrated that subsurface hydrologic model structure and  
47 parameterization can significantly affect simulated land-atmosphere exchanges [*Condon et al.*,  
48 2013; *Hou et al.*, 2012; *Kollet and Maxwell*, 2008; *Miguez-Macho and Fan*, 2012] and therefore  
49 boundary layer dynamics [*Maxwell and Miller*, 2005; *Rihani et al.*, 2015], cloud formation  
50 [*Rahman et al.*, 2015], and climate [*Leung et al.*, 2011; *Taylor et al.*, 2013]. Lateral subsurface  
51 processes are fundamentally important at multiple spatial scales, including hill-slope scales  
52 [*McNamara et al.*, 2005; *Zhang et al.*, 2011], basin scales in semi-arid and arid climates where  
53 regional aquifers sustain baseflows in rivers [*Schaller and Fan*, 2009], and wetlands [*Fan and*  
54 *Miguez-Macho*, 2011]. However, some current-generation land surface models (LSMs) routinely  
55 omit explicit lateral subsurface processes [*Clark et al.*, 2015; *Kollet and Maxwell*, 2008; *Nir et*  
56 *al.*, 2014], while others include them (described below). Observational and modeling studies  
57 suggest that groundwater forms an environmental gradient in soil moisture availability by  
58 redistributing water that could profoundly shape critical zone evolution at continental to global  
59 scales [*Fan et al.*, 2013; *Taylor et al.*, 2013]. The mismatch between observed and simulated  
60 evapotranspiration by current LSMs could be explained by the absence of lateral groundwater  
61 flow [*Maxwell and Condon*, 2016].

62 It has been increasingly recognized that rivers, despite their small aerial extent on the  
63 landscape, play important roles in watershed functioning through their connections with  
64 groundwater aquifers and riparian zones [*Shen et al.*, 2016]. The interactions between  
65 groundwater and river water prolong physical storage and enhance reactive processing that alter  
66 water chemistry, downstream transport of materials and energy, and biogenic gas emissions  
67 [*Fischer et al.*, 2005; *Harvey and Gooseff*, 2015]. The Earth System modeling community  
68 recognizes such a gap in existing Earth system models and calls for improved representation of  
69 biophysical and biogeochemical processes within the terrestrial-aquatic interface [*Gaillardet et*  
70 *al.*, 2014].

71 Over the past decade, much effort has been expended to include groundwater into LSMs.  
72 Groundwater is important to water and energy budgets such as evapotranspiration (ET), latent  
73 heat (LH), and sensible heat (SH), but also to biogeochemical processes such as gross primary  
74 production, heterotrophic respiration, and nutrient cycling. The lateral convergence of water  
75 along the landscape and two-way groundwater-surface water exchange are identified as the most

76 relevant subsurface processes to large-scale Earth System functioning (see review by *Clark et al.*  
77 [2015]). However, the choice of processes, the approaches to represent multi-scale structures and  
78 heterogeneities, the data and computational demands, etc., all vary greatly among the research  
79 groups even working on the same land models.

80 Most of the LSMs reviewed by *Clark et al.* [2015] do not explicitly account for stream-  
81 aquifer-land interactions. For example, the Community Land Model version 4.5 allows for  
82 reinfiltration of flooded waters in a highly parameterized way without explicitly linking to  
83 groundwater dynamics, therefore only one-way flow from the aquifer to the stream is simulated  
84 [*Oleson et al.*, 2013]. The Land-Ecosystem-Atmosphere Feedback model treats river elevation as  
85 part of the 2-D vertically integrated groundwater flow equation and allows river and floodwater  
86 to infiltrate through sediments in the flood plain [*Miguez-Macho and Fan*, 2012].

87 In contrast, the fully integrated models, being a small subset of LSMs, explicitly represent  
88 the two-way exchange between groundwater aquifers and their adjacent rivers in a spatially  
89 resolved fashion. Such models couple a completely integrated hydrology model with a land  
90 surface model, so that the surface-water recharge to groundwater by infiltration or intrusion and  
91 base flow discharge from groundwater to surface waters can be estimated in a more mechanistic  
92 way.

93 Examples of the integrated models include: (1) the coupling between the Common Land  
94 Model (CoLM) and a variably saturated groundwater model (ParFlow) [*Maxwell and Miller*,  
95 2005]; (2) the Penn State Integrated Hydrologic Model (PIHM) [*Shi et al.*, 2013]; (3) the  
96 coupling between the Process-based Adaptive Watershed Simulator (PAWS) and CLM4.5 [*Ji et*  
97 *al.*, 2015; *Pau et al.*, 2016; *Riley and Shen*, 2014]; (4) the coupling between the CATchment  
98 Hydrology (CATHY) model and the Noah model with multiple parameterization schemes  
99 (Noah-MP) [*Niu et al.*, 2014]; and (5) the coupling between CLM3.5 and ParFlow through the  
100 Ocean Atmosphere Sea Ice Soil external coupler (OASIS3) in the Terrestrial Systems Modeling  
101 Platform (TerrSysMP) [*Shrestha et al.*, 2014; *Gebler et al.*, 2017]. The integrated models  
102 eliminate the need for parameterizing lateral groundwater flow and allow the interconnected  
103 groundwater–surface-water systems to evolve dynamically based on the governing equations and  
104 the properties of the physical system. Although such models often require robust numerical  
105 solvers on high-performance computing (HPC) facilities to achieve high-resolution, large-extent  
106 simulations [*Maxwell et al.*, 2015], they have been increasingly applied for hydrologic prediction

107 and environmental understanding. However, as a result of difference in physical process  
108 representations and numerical solution approaches in terms of (1) the coupling between the  
109 variably saturated groundwater and surface water flow; (2) representation of surface water flow;  
110 and (3) implementation of subsurface heterogeneity in the existing integrated models,  
111 significant discrepancies exist in their results when the models were applied to highly nonlinear  
112 problems with heterogeneity and complex water table dynamics, while many of the models show  
113 good agreement for simpler test cases where traditional runoff generation mechanisms (i.e.,  
114 saturation and infiltration excess runoff) apply [Kollet *et al.*, 2017; Maxwell *et al.*, 2014].

115 The developments of the integrated models have enabled scientific explorations of  
116 interactions and feedback mechanisms in the aquifer-soil-vegetation-atmosphere continuum  
117 using a holistic and physically based approach [Shrestha *et al.*, 2014; Gilbert *et al.*, 2017].  
118 Compared to simulations of regional climate models coupled to traditional LSMs, such a  
119 physically based approach shows less sensitivity to uncertainty in the subsurface hydraulic  
120 characteristics that could propagate from deep subsurface to free troposphere [Keune *et al.*,  
121 2016], while other physical representations (e.g., parameterizations in evaporation and  
122 transpiration, atmospheric boundary layer schemes) could have significant effects on the  
123 simulations as well [Sulis *et al.*, 2017]. Therefore, it is of great scientific interest to further  
124 develop the integrated models and benchmarks to achieve improved understanding of complex  
125 interactions in the fully coupled Earth system.

126 Motivated by the great potentials of using an integrated model to explore Earth system  
127 dynamics, the objective of this study is three-fold. First, we aim to document the development of  
128 a coupled land surface and subsurface model as a first step toward a new integrated model,  
129 featuring the two-way coupling between two highly-scalable and state-of-the-art open-source  
130 codes: CLM4.5 [Oleson *et al.*, 2013] and a reactive transport model PFLOTRAN [Lichtner *et al.*,  
131 2015]. The coupled model mechanistically represents the two-way exchange of water and solute  
132 mass between aquifers and river, as well as land-atmosphere exchange of water and energy. The  
133 coupled model is therefore named as CP v1.0 hereafter. We note that in recent years, efforts have  
134 been made to implement carbon–nitrogen decomposition, nitrification, denitrification, and plant  
135 uptake from CLM4.5 in the form of a reaction network solved by PFLOTRAN to enable the  
136 coupling of biogeochemical processes between the two models [Tang *et al.*, 2016]. In addition,  
137 although PAWS is coupled to the same version of CLM (i.e., CLM4.5) [Ji *et al.*, 2015; Pau *et*

138 *al.*, 2016], PFLOTRAN resolves the subsurface in a 3-D fashion, while PAWS approximates the  
139 3D Richards equation by divide the subsurface into an unsaturated domain represented by the 1-  
140 D Richards Equation coupled with 3D saturated groundwater flow equation for subsurface flow,  
141 by assuming that there is no horizontal flow in unsaturated portion of soil, and that lateral flux in  
142 saturated portion is evenly distributed.

143 Second, we describe a numerically challenging benchmarking case for verifying coupled land  
144 surface and subsurface models, featuring a highly dynamic river boundary condition determined  
145 by dam-induced river stage variations (Hauer et al., 2017), representative of managed river  
146 reaches that are of global significance as a result of dam constructions in the past few decades  
147 [Zhou et al., 2016]. Third, we assess the effects of spatial resolution and projected hydro-climatic  
148 changes on simulated land surface fluxes and exchange of groundwater and river water using the  
149 coupled model and datasets from the benchmarking case. In section 2, we describe the  
150 component models and our coupling strategy. In section 3, we describe an application of the  
151 model to a field site along the Hanford reach of the Columbia River, where the subsurface  
152 properties are well characterized and long-term monitoring of river stage, groundwater table, and  
153 exchange of groundwater and river water exist. In section 4, we assess the effects of spatial  
154 resolution and hydro-climatic conditions to simulated fluxes and state variables. In section 5,  
155 conclusion and future work are discussed.

156

## 157 **2 Model description**

### 158 **2.1 The Community Land Model version 4.5**

159 CLM4.5 [Oleson et al., 2013] is the land component of the Community Earth System Model  
160 version 1 (CESM1) [Hurrell et al., 2013], a fully coupled numerical simulator of the Earth  
161 system consisting of atmospheric, ocean, ice, land surface, carbon cycle, and other components.  
162 It has been applied successfully to explore interactions among water, energy, carbon, and  
163 biogeochemical cycling at local to global scales [Leng et al., 2016b; Xu et al., 2016], and proven  
164 to be highly scalable on leading HPC facilities such as the U.S. Department of Energy  
165 (USDOE)'s National Energy Research Scientific Computing Center (NERSC). The model  
166 includes parameterizations of terrestrial hydrological processes including interception,  
167 throughfall, canopy drip, snow accumulation and melt, water transfer between snow layers,

168 infiltration, evaporation, surface runoff, sub-surface drainage, redistribution within the soil  
169 column, and groundwater discharge and recharge to simulate changes in canopy water, surface  
170 water, snow water, soil water, and soil ice, and water in the unconfined aquifer [Oleson *et al.*,  
171 2013]. Precipitation is either intercepted by the canopy, falls directly to the snow/soil surface  
172 (throughfall), or drips off the vegetation (canopy drip). Water input at the land surface, the sum  
173 of liquid precipitation reaching the ground and melt water from snow, is partitioned into surface  
174 runoff, surface water storage, and infiltration into the soil. Two sets of runoff generation  
175 parameterizations, including formulations for saturation and infiltration excess runoff and  
176 baseflow, are implemented into the model: the TOPMODEL-based runoff generation  
177 formulations [Beven and Kirkby, 1979; Niu *et al.*, 2005; Niu *et al.*, 2007] and the Variable  
178 Infiltration Capacity (VIC)-based runoff generation formulations [Lei *et al.*, 2014; Liang *et al.*,  
179 1994; Wood *et al.*, 1992]. Surface water storage and outflow in and from wetlands and small sub-  
180 grid scale water bodies are parameterized as functions of fine-spatial-scale elevation variations  
181 called microtopography. Soil water is predicted from a multi-layer model based on the 1-D  
182 Richards equation, with boundary conditions and source/sink terms specified as infiltration,  
183 surface and sub-surface runoff, gradient diffusion, gravity, canopy transpiration through root  
184 extraction, and interactions with groundwater. A groundwater component is added in the form of  
185 an unconfined aquifer lying below the soil column following Niu *et al.* [2007]. The model  
186 computes surface energy fluxes following the Monin-Obukhov Similarity Theory using  
187 formulations in Zeng *et al.* (1998), which updates the calculation of boundary resistance to  
188 account for understory turbulence, sparse and dense canopies, and surface litter layer (Sakaguchi  
189 and Zeng, 2009; Zeng *et al.*, 2005; Zeng and Wang, 2007). Water and energy budgets are  
190 conserved at every modeling step.

## 191 **2.2 PFLOTRAN**

192 PFLOTRAN is a massively-parallel multi-physics simulator [Hammond *et al.*, 2014] developed  
193 and distributed under an open source GNU LGPL license and is freely available through  
194 Bitbucket ((<https://bitbucket.org/pflotran/pflotran>)). It solves a system of generally nonlinear  
195 partial differential equations (PDEs) describing multiphase, multicomponent and multiscale  
196 reactive flow and transport in porous materials. The PDEs are spatially discretized using a finite  
197 volume technique, and the backward Euler scheme is used for implicit time discretization. It has

198 been widely used for simulating subsurface multiphase flow and reactive biogeochemical  
 199 transport processes [*Chen et al.*, 2013; *Chen et al.*, 2012; *Hammond and Lichtner*, 2010;  
 200 *Hammond et al.*, 2011; *Kumar et al.*, 2016; *Lichtner and Hammond*, 2012; *Liu et al.*, 2016; *Pau*  
 201 *et al.*, 2014]

202 PFLOTRAN is written in object-oriented Fortran 2003/2008 and relies on the PETSc  
 203 framework [*Balay et al.*, 2015] to provide the underlying parallel data structures and solvers for  
 204 scalable high performance computing. PFLOTRAN uses domain decomposition and MPI  
 205 libraries for parallelization. PFLOTRAN has been run on problems composed of over 3 billion  
 206 degrees of freedom with up to 262,144 processors, but it is more commonly employed on  
 207 problems with millions to tens of millions of degrees of freedom utilizing hundreds to thousands  
 208 of processors. Although PFLOTRAN is designed for massively parallel computation, the same  
 209 code base can be run on a single processor without recompiling, which may limit problem size  
 210 based on available memory.

211 In this study, PFLOTRAN is used to simulate single phase variably saturated flow and solute  
 212 transport in the subsurface. Single-phase variably saturated flow is based on the Richards  
 213 equation with the form

$$214 \quad \frac{\partial}{\partial t}(\varphi s \rho) + \nabla \cdot \rho \mathbf{q} = 0, \quad (1)$$

215 with liquid density  $\rho$ , porosity  $\varphi$ , and saturation  $s$ . The Darcy velocity,  $\mathbf{q}$ , is given by

$$216 \quad \mathbf{q} = -\frac{k k_r}{\mu} \nabla(p - \rho g z), \quad (2)$$

217 with liquid pressure  $p$ , viscosity  $\mu$ , acceleration of gravity  $g$ , intrinsic permeability  $k$ , relative  
 218 permeability  $k_r$ , and elevation above a given datum  $z$ . Conservative solute transport in the liquid  
 219 phase is based on the advection-dispersion equation

$$220 \quad \frac{\partial}{\partial t}(\varphi s C) + \nabla \cdot (\mathbf{q} - \varphi s D \nabla) C = 0, \quad (3)$$

221 with solute concentration  $C$  and hydrodynamic dispersion coefficient  $D$ . The discrete system of  
 222 nonlinear PDEs for flow and transport are solved using the Newton-Raphson method.

## 223        **2.3 Model coupling**

224        In this study, CLM4.5's one-dimensional models for flow in unsaturated [Zeng and Decker,  
225        2009] and saturated [Niu et al., 2007] zones are replaced by PFLOTRAN's RICHARDS mode to  
226        simulate unsaturated-saturated flow within the three-dimensional subsurface domain. Although  
227        PFLOTRAN is also capable of simulating coupled flow and thermal processes in the subsurface  
228        including explicit representation of liquid-ice phase [Karra et al., 2014], as well as, soil nutrient  
229        cycles [Hammond and Lichtner, 2010; Zachara et al., 2016; Tang et al., 2016], those processes  
230        are not coupled between the two models in this study. A schematic representation of the coupling  
231        between CLM4.5 and PFLOTRAN is shown in Figure 1. A model coupling interface based on  
232        PETSc data structures was developed to couple the two models and the interface includes some  
233        key design features of the CESM coupler [Craig et al., 2012]. The model coupling interface  
234        allows each model grid to have a different spatial resolution and domain decomposition across  
235        multiple processors. While CLM4.5 uses a round-robin decomposition approach, PFLOTRAN  
236        employs domain decomposition via PETSc (Figure 1a). Interpolation of gridded data from one  
237        model onto the grids of the other is done through sparse matrix vector multiplication. As a  
238        preprocessing step, sparse weight matrices for interpolating data between the two models are  
239        saved as mapping files. Analogous to the CESM coupler, the mapping files are saved in a format  
240        similar to the mapping files produced by the ESMF\_RegridWeightGen  
241        (<https://www.earthsystemcog.org/projects/regridweightgen>). ESMF regriding tools provide  
242        multiple interpolation methods (conservative, bilinear, and nearest neighbor) to generate the  
243        sparse weight matrix.

244        In this work, we have used a conservative remapping method to interpolate data between  
245        CLM and PFLOTRAN. During model initialization, the model coupling interface first  
246        collectively reads all required sparse matrices. Next, the model coupling interface reassembles  
247        local sparse matrices after accounting for domain decomposition of each model (figures 1b and  
248        1c). . For a given time step, CLM4.5 first computes infiltration, evaporation, and transpiration  
249        within the domain and then sends the data to the model coupling interface. The model coupling  
250        interface for each processor receives relevant CLM data vector from all other processors;  
251        interpolates data from CLM's grid onto PFLOTRAN's grid via a local sparse matrix vector  
252        multiplication; and saves the resulting vector in PFLOTRAN's data structures as prescribed flow  
253        conditions (Figure 1b). PFLOTRAN evolves the subsurface states over the given time step

254 length. The updated soil moisture simulated by PFLOTRAN are then provided back to the model  
255 coupling interface, which interpolates data from PFLOTRAN's grid onto CLM's grid (Figure  
256 1c). The interpolated data is saved in CLM4.5's data structure and used for simulating land  
257 water- and energy- budget terms in the next step. Figure 2 shows a schematic representation of  
258 how stream-aquifer-land interactions are simulated in CP v1.0 when applied to the field scale,  
259 such as the 300 Area domain to be introduced in section 3.1.

260

### 261 **3 Site description and model configuration**

#### 262 **3.1 The Hanford site and the 300 Area**

263 The Hanford Reach is a stretch of the lower Columbia River extending approximately 55 km  
264 from the Priest Rapids hydroelectric dam to the outskirts of Richland, Washington, USA (Figure  
265 3a) [Tiffan *et al.*, 2002]. The Columbia River above Priest Rapids Dam drains primarily  
266 mountainous regions in Canada, Idaho, Montana, and Washington, over which spatio-temporal  
267 distributions of precipitation and snowmelt modulate the timing and magnitude of river flows  
268 [Elsner *et al.*, 2010; Hamlet and Lettenmaier, 1999]. The Columbia River is highly regulated by  
269 dams for power generation and river stage and discharge along the Hanford Reach displays  
270 significant variation on multiple time scales. Strong seasonal variations occur with the greatest  
271 discharge (up to  $12,000 \text{ m}^3 \text{ s}^{-1}$ ) occurring from May through July due to snow melt, with less  
272 discharge ( $>1,700 \text{ m}^3 \text{ s}^{-1}$ ) and lower flows occurring in the fall and winter [Hamlet and  
273 Lettenmaier, 1999; Waichler *et al.*, 2005]. Significant variation in discharge also occurs on a  
274 daily or hourly basis due to power generation, with fluctuations in river stage of up to 2 m within  
275 a 6-24 hr period being common [Tiffan *et al.*, 2002].

276 The Hanford site features an unconfined aquifer developed in Miocene-Pliocene fluvial and  
277 lacustrine sediments of the Ringold Formation, overlain by Pleistocene flood gravels of the  
278 Hanford formation [Thorne *et al.*, 2006] that is in hydrologic continuity with the Columbia  
279 River. The Hanford formation gravel and sand, deposited by glacial outburst floods at the end of  
280 the Pleistocene [Bjornstad, 2007], has a high average hydraulic conductivity at  $\sim 3,100 \text{ m day}^{-1}$   
281 [Williams *et al.*, 2008]. The fluvial deposits of the Ringold Formation have much lower  
282 hydraulic conductivity than the Hanford but are still relatively conductive at  $36 \text{ m day}^{-1}$

283 [Williams *et al.*, 2008]. Fine-grained lacustrine Ringold silt has a much lower estimated  
284 hydraulic conductivity of  $1 \text{ m day}^{-1}$ . The hydraulic conductivity of recent alluvium lining the  
285 river channel is low relative to the Hanford formation, which tends to dampen the response of  
286 water table elevation in wells near the river when changes occur in river stage [Hammond *et al.*,  
287 2011; Williams *et al.*, 2008]. Overall, the Columbia River through the Hanford Reach is a prime  
288 example of a hyporheic corridor with an extensive floodplain aquifer. It is consequently an ideal  
289 alluvial system for evaluating the capability of the coupled model in simulating stream-aquifer-  
290 land interactions.

291 The region is situated in a cold desert climate with temperatures, precipitation, and winds that  
292 are greatly affected by the presence of mountain barriers. The Cascade Range to the west creates  
293 a strong rain shadow effect by forming a barrier to moist air moving from the Pacific Ocean,  
294 while the Rocky Mountains and ranges to the north protect it from the more severe cold polar air  
295 masses and winter storms moving south across Canada. Meteorological data are collected by the  
296 Hanford Meteorological Monitoring Network (<http://www.hanford.gov/page.cfm/hms>), which  
297 collects meteorological data representative of the general climatic conditions for the Hanford  
298 site.

299 A segment of the hyporheic corridor in the Hanford 300 Area (300A) was chosen to evaluate  
300 the model's capability in simulating river-aquifer-land interactions. Located at the downstream  
301 end of the Hanford Reach, the impact of dam operations on river stage is relatively damped,  
302 exhibiting a typical variation of  $\sim 0.5 \text{ m}$  within a day and 2-3 m in a year. The study domain  
303 covers an area of  $400 \text{ m} \times 400 \text{ m}$  along the Columbia River shoreline (Figure 3b). Aquifer  
304 sediments in the 300 Area are coarse grained and highly permeable [Chen *et al.*, 2013;  
305 Hammond and Lichtner, 2010]. Coupled with dynamic river stage variations, the resulting  
306 system is characterized by stage-driven intrusion and retreat of river water into the adjacent  
307 unconfined aquifer system. During high-stage spring runoff events, river water has been detected  
308 in monitoring wells nearly 400 m from the shoreline [Williams *et al.*, 2008]. During baseline,  
309 low-stage conditions (October-February), the Columbia River is a gaining stream, and the  
310 aquifer pore space is occupied by groundwater.

311 The study domain is instrumented with groundwater monitoring wells (Figure 3b) and a river  
312 gaging station that records water table elevations. A vegetation survey in 2015 was conducted to  
313 provide aerial coverages of grassland, shrubland, riparian trees in the domain (Figure 3b). A

314 high-resolution topography and bathymetry dataset at 1-m resolution was assembled from  
315 multiple surveys by *Coleman et al.* [2010]. The data layers originated from Deep Water  
316 Bathymetric Boat surveys, terrestrial Light Detection and Ranging (LiDAR) surveys, and special  
317 hydrographic LiDAR surveys penetrating through water to collect both topographic and  
318 bathymetric elevation data.

### 319 **3.2 Model configuration, numerical experiments, and analyses**

320 To assess the effect of spatial resolution on simulated variables such as latent heat, sensible heat,  
321 water table depth, and river water in the domain, we configured CP v1.0 simulations at three  
322 horizontal spatial resolutions: 2-m, 10-m, and 20-m over the 400 m×400 m domain, respectively.  
323 For comparison purposes, we also configured a 2-m-resolution CP v1.0 vertical only simulation  
324 (i.e.,  $S_{v2m}$ ) in which lateral transfers of flow and solutes in the subsurface are disabled. Due to  
325 lack of observations of water and energy fluxes from the land surface, in this study we treat the  
326 2-m-resolution CP v1.0 as the baseline and compare simulation results at other resolutions to it.  
327 New hydrologic regimes are projected to emerge over the Pacific Northwest in as early as the  
328 2030s due to increases in winter precipitation and earlier snow melt in response to future  
329 warming [*Leng et al.*, 2016a]. Therefore, we expect that spring and early summer river discharge  
330 along the reach might increase in the future. To evaluate how land surface-subsurface coupling  
331 might be modulated hydro-climatic conditions, we designed additional numerical experiments by  
332 driving the model with elevated river stages by adding five meters to the observed river stage  
333 time series. The simulations and their configurations are summarized in Table 1.

334 The PFLOTRAN subsurface domain, also terrain-following and extending from soil surface  
335 (including riverbed) to 32 m below the surface, was discretized using a structured approach with  
336 rectangular grids. For the 2-m, 10-m, and 20-m resolution simulations, each mesh element was 2  
337 m × 2 m, 10 m × 10 m, and 20 m×20 m, in the horizontal direction, and 0.5 m in the vertical  
338 direction, giving  $2.56 \times 10^6$ ,  $99.2 \times 10^3$ , and  $2.48 \times 10^3$  control volumes in total. The domain  
339 contained two materials with contrasting hydraulic conductivities: Hanford and Ringold (Figure  
340 4). Note that only the soil moisture and soil hydraulic properties within the top 3.8 m are  
341 transferred from PFLOTRAN to CLM4.5 to allow simulations of infiltration, evaporation, and  
342 transpiration in the next time step, as the CLM4.5 subsurface domain is limited to 3.8 meters and  
343 cannot currently be easily modified. The hydrogeological properties of the Hanford and Ringold

344 materials (Table 2) were taken from *Williams et al.* [2008]. The unsaturated hydraulic  
345 conductivity in PFLTORAN simulations was computed using the Van Genuchten water retention  
346 function [*van Genuchten*, 1980] and the Burdine permeability relationship [*Burdine*, 1953].

347 We applied time varying pressure boundary conditions to PFLOTTRAN's subsurface domain  
348 at the northern, western, and southern boundaries. The transient boundary conditions were  
349 derived using kriging-based interpolations of hourly water table elevation measurements in wells  
350 inside and beyond the model domain, following the approach used by *Chen et al.* [2013].  
351 Transient head boundary conditions were applied at the eastern boundary with water table  
352 elevations from the river gaging station and the gradient along the river estimated using water  
353 elevations simulated by a 1-D hydraulic model along the reach, the Modular Aquatic Simulation  
354 System in 1-Dimension (MASS1) [*Waichler et al.*, 2005], with a Nash–Sutcliffe coefficient  
355 [*Nash and Sutcliffe*, 1970] of 0.99 in the simulation period (figure not shown). The river stage  
356 simulated by MASS1 was also used to fill river stage measurement gaps caused by instrument  
357 failures. A conductance value of  $10^{-12}$  m was applied to the eastern shoreline boundary to mimic  
358 the damping effect of low-permeability material on the river bed [*Hammond and Lichtner*,  
359 2010]. A no-flow boundary condition was specified at the bottom of the domain to represent the  
360 basalt underlying the Ringold formation.

361 Vegetation types (Figure 3b) were converted to corresponding CLM4.5 plant functional types  
362 (PFTs) and bare soil (Figure 5). At each resolution, fractional area coverages of PFTs and bare  
363 soil are determined based on the base map and written into the surface dataset as CLM4.5 inputs  
364 (figures 5, S1, and S2). The CLM4.5 domain is terrain-following by treating the land surface as  
365 the top of the subsurface domain, which is hydrologically active to a depth of 3.8 m. The  
366 topography of the domain is retrieved from the 1-m topography and bathymetry dataset  
367 [*Coleman et al.*, 2010] based on the North American Vertical Datum of 1988 (NAD88) and  
368 resampled to each resolution (Figure S3).

369 The simulations were driven by hourly meteorological forcing from the Hanford  
370 meteorological stations and hourly river stage from the gaging station over the period of 2009-  
371 2015. Precipitation, wind speed, air temperature, and relative humidity were taken from the 300  
372 Area meteorological station (longitude  $119.726^{\circ}$ , latitude  $46.578^{\circ}$ ), located  $\sim 1.5$  km from the  
373 modeling domain. Other meteorological variables, such as downward shortwave and longwave

374 radiation, were obtained from the Hanford Meteorological station (longitude 119.599°, latitude  
375 46.563°) located in the center of the Hanford site. The first two years of simulations (i.e., 2009  
376 and 2010) were discarded as the spin-up period, so that 2011-2015 is treated as the simulation  
377 period in the analyses.

378 Among the hydro-climatic forcing variables (e.g., river stage, surface air temperature,  
379 incoming shortwave radiation, and total precipitation), river stage displayed the greatest inter-  
380 annual variability (Figure 6). During the study period, high river stages occurred in early summer  
381 of 2011 and 2012 due to the melt of above-average winter snow packs in the upstream drainage  
382 basin, typical flow conditions occurred in 2013 and 2014, while 2015 was a year with low  
383 upstream snow accumulation. Meanwhile, the meteorological variables, especially temperature  
384 and shortwave radiation, do not show much inter-annual variability or trend, while precipitation  
385 in late spring (i.e., May) of 2012 is higher than that in the other years, coincident with the high  
386 river stage in 2012. In the “elevated” experiments (i.e.,  $S_{E2m}$ ,  $S_{E10m}$ , and  $S_{E20m}$ ), the observed  
387 river stage (meters based on NAD88) was increased by five meters at each hourly time step to  
388 mimic a perturbed hydro-climatic condition in response to future warming.

389 To evaluate effects of river water and groundwater exchanges on land surface energy  
390 partitioning, we separated the study domain for the 2-m simulations with lateral water exchange  
391 (i.e.,  $S_{2m}$  and  $S_{E2m}$ ) into two sub-domains based on 2-m topography (shown in Figure S3a): (a)  
392 the inland domain where the surface elevation is higher than 110 m; and (b) the riparian zone  
393 where the surface elevation is less than or equal to 110 m. In addition to the latent heat flux, the  
394 evaporative fraction, defined as the ratio of the latent heat flux to the sum of latent and sensible  
395 heat fluxes was calculated over the sub-domains for both observed and elevated conditions at a  
396 daily time step for all days with significant energy inputs (i.e., when net radiation is greater than  
397  $50 \text{ W m}^2$ ). The evaporative is an indicator of the type of surface as summarized in literature  
398 [Lewis, 1995]: it is typically less than one over surfaces with abundant water supplies, ranges  
399 between 0.75-0.9, 0.5-0.7, 0.15-0.3 for tropical rainforests, temperate forests and grasslands,  
400 semi-arid landscapes, respectively, and approaches 0 over deserts.

401 To better quantify the spatio-temporal dynamics of stream-aquifer interactions, a  
402 conservative tracer with a mole fraction of one was applied at the river boundary to track the flux  
403 of river water and its total mass in the subsurface domain. While a constant concentration was

404 maintained at the river (i.e., eastern) boundary, the tracer was allowed to be transported out of  
405 the northern, western, and southern boundaries. Water infiltrating at the upper boundary based on  
406 CLM4.5 simulations was set to be tracer free, while a zero-flux tracer boundary condition was  
407 applied at the lower boundary. The initial flow condition was a hydrostatic pressure distribution  
408 based on the water table, as interpolated from the same set of wells that were used to create the  
409 transient lateral flow boundary conditions at the northern, western, and southern boundaries. The  
410 initial conservative tracer concentration was set to be zero for all mesh elements in the domain.  
411 The simulations were started on 1 January 2009 and the first two years were discarded as the  
412 spin-up period in the analysis. The mass of tracers in the domain and the fluxes of tracers across  
413 the boundary allow us to quantitatively understand how river water is retained and transported in  
414 the subsurface domain.

415 A standalone CLM4.5 simulation was also configured and performed (i.e., CLM<sub>2m</sub> in Table  
416 1). CLM<sub>2m</sub> shared the same subsurface properties and initial conditions as the CLM4.5 setup in  
417 S<sub>2m</sub> and S<sub>v2m</sub> where CP v1.0 were used. However, we note that CLM<sub>2m</sub> are not directly  
418 comparable to other simulations listed in Table 1 for following reasons: (1) The CLM4.5  
419 simulates subsurface hydrologic processes only up to 3.8 m below the surface, while in the CP  
420 v1.0 subsurface domain extends up to ~30 m below the surface; (2) as discussed in section 2.1,  
421 CLM4.5 uses TOPMODEL-based parameterizations to simulate surface and subsurface runoffs,  
422 as well as mean groundwater table depth using formulations derived from catchment hydrology  
423 that are only applicable at coarser resolutions; (3) The key hydrologic processes (i.e., the  
424 exchange of river water and groundwater at the east boundary and lateral transfer of water at all  
425 other boundaries) that affect the hydrologic budget of the system are missing from CLM4.5.  
426 Therefore, the simulated latent heat fluxes from CLM<sub>2m</sub> are only provided as a reference for  
427 interested readers in Figure S4 and were not analyzed in section 4.

428

## 429 **4 Results**

### 430 **4.1 Model evaluation**

431 For the 3-D numerical experiments driven by the observed river stage time series (i.e., S<sub>2m</sub>,  
432 S<sub>10m</sub>, S<sub>20m</sub>), CP v1.0 simulated soil water pressure was converted to water table depth and

433 compared against observed values at selected wells that were distributed throughout the domain  
434 and of variable distances from the river (Figures 7, S5 and Table 3). The model performed very  
435 well in simulating the temporal dynamics of the water table at all resolutions. The root-mean-  
436 square errors were 0.028 m, 0.028 m, and 0.023 m at 2-m, 10-m, and 20-m resolutions,  
437 respectively. The corresponding Nash–Sutcliffe coefficients were 0.998, 0.998, and 0.999. It was  
438 surprising that the performance metrics at 20-m resolution matches the observations better than  
439 those at finer resolutions, but the differences were marginal given the close match between the  
440 model simulation results and observations. River stage was clearly the dominant driving factor  
441 for water table fluctuations at the inland wells. In addition, errors in water and tracer budget  
442 conservations, and surface energy conservation for each time step in  $S_{2m}$  are shown in figures  
443 S6a, b, and c respectively. The errors are sufficiently small when compared to the magnitudes of  
444 the related fluxes to ensure faithful simulations in CP v1.0. These results indicated that the  
445 coupled model was capable of simulating dynamic stream-aquifer interactions in the near shore  
446 groundwater aquifer that experiences pressure changes induced by river stage variations at sub-  
447 daily time scales. Effect of stream-aquifer interactions on land surface energy partitioning

448 Next we evaluated the role of water table fluctuations on land surface variables, including  
449 latent heat (LH) and sensible heat (SH) fluxes. The site is characterized by an approximate 10 m  
450 vadose zone and surface fluxes and groundwater dynamics are typically decoupled [*Maxwell and*  
451 *Kollet, 2008*], especially over the inland portion of the domain covered by shallow-rooted PFTs  
452 and with higher surface elevations. However, river discharge and water table elevation displayed  
453 large seasonal and inter-annual variability in the study period. Therefore, we selected the month  
454 of June in each year to assess potential land surface-groundwater coupling because it is the  
455 month of peak river stage, while energy input is high and relatively constant across the years  
456 (Figure 8a).

457 In June 2011 and 2012, high river stages push the groundwater table to ~108 m (or ~6 m  
458 below the land surface). Groundwater at that elevation can affect land surface water and energy  
459 exchanges with the atmosphere. The shrubs, including the patch of Basin big sagebrush and the  
460 mixture of rabbitbrush and bunchgrass on the slope close to the river, are able to tap into the  
461 elevated water table with their deeper roots. In the inland portion of the domain, capillary supply  
462 was most evident in high-water years (i.e., 2011 and 2012), remains influential in normal years  
463 (i.e., 2013 and 2014), and is essentially disabled in low-water years (i.e., 2015). The lateral

464 discharge of shallow groundwater to the river led to a band of negative difference in LH between  
465  $S_{2m}$  and  $S_{v2m}$  at the river boundary when the stage was low due to a decrease in rooting zone soil  
466 moisture for evapotranspiration by the riparian trees (Figure 8b). This pattern was most evident  
467 in June 2015. Such a mechanism decreases in high-water and normal years because of more  
468 frequent inundation of the river bank and groundwater gradient reversal.

469 Driven by elevated river stages, land surface energy partitioning in  $S_{E2m}$  (figures 9 and 10)  
470 was significantly shifted from that in  $S_{2m}$  (Figure 8a) through two mechanisms: (1) expanding  
471 the periodically inundated fraction of the riparian zone (i.e., surface elevation  $\leq 110$  m); and (2)  
472 enhancing moisture availability in the vadose zone in the inland domain (i.e., surface elevation  $>$   
473 110 m) through capillary rise. Both mechanisms led to general increases in simulated vadose-  
474 zone moisture availability and therefore higher latent heat fluxes compared to the simulations  
475 driven by the observed condition. For the inland domain, evaporative fraction clearly displayed  
476 an increasing trend as the groundwater table level becomes shallower, consistent between the  
477 simulations (Figure 10c). The daily evaporative fractions for the inland domain stayed well  
478 below 0.2 when the water table levels are less than 112 m, suggesting decoupled surface-  
479 subsurface conditions in a typical semi-arid environment. When water table levels increased to  
480 be above 112 m, the evaporative fraction increases to  $\sim 0.2$ , indicating that the surface and  
481 subsurface processes become more strongly coupled because of improved water availability for  
482 evapotranspiration, especially in the elevated simulation (i.e.,  $S_{E2m}$ ). Evaporative fraction in the  
483 riparian zone remained close to 1.0, suggesting strong influences of the river and the role of  
484 deeper rooted plant types (e.g., riparian trees and shrubs) in modulating the energy partitioning  
485 (Figure 10d) of riparian zones in the semi-arid to arid environments.

486 To confirm the above findings, the liquid saturation [*unitless*] and mass of river water [*mol*]  
487 in the domain from  $S_{2m}$  and  $S_{E2m}$  on 30 June each year are plotted along a transect perpendicular  
488 to the river ( $y = 200$  m) in figures 11 and S7, and across a x-y plane at an elevation of 107 m in  
489 figures S8 and S9, respectively. Driven by the pressure introduced by elevated river stages, river  
490 water not only intruded further toward or even across the western boundary in high water years,  
491 but also led to shallower water table and increased liquid saturation in the vadose zone due to  
492 capillary rise across the domain. In fact, liquid saturation in the shallow vadose zone could  
493 increase from 0.1-0.2 in  $S_{2m}$  to 0.3-0.4 in  $S_{E2m}$  on these days because of river water intrusion.  
494 The river-water tracer could show up in the near-surface vadose zone at a distance of  $\sim 400$  m

495 from the river (Figure S7). Interestingly, by comparing the spatial distributions of river-water  
496 tracer in the low-water year (i.e., 2015) between the “observed” and “elevated” scenarios, the  
497 presence of river water in the domain was much less in the elevated scenario in terms of its  
498 spatial coverage (figures 11 and S7). This pattern suggests that after a number of years of  
499 enhanced river water intrusion into the domain, the hydraulic gradient between groundwater and  
500 river-water could be reversed, so that groundwater discharging might be expected more  
501 frequently in low-water years in a prolonged elevated scenario.

502 The responses of LH and evaporative fraction (figures 9 and 10) indicated that a tight  
503 coupling among stream, aquifer, and land surface processes occurred in the elevated scenario,  
504 which could become realistic in one to two decades for the study site, or for other sites along the  
505 Hanford reach characterized by lower elevations under the current condition.

#### 506 **4.2 Effect of spatial resolution**

507 To apply the model to large-scale simulations or over a long time period, it is important to assess  
508 how the model performs at coarser resolution, as the 2-m simulations are computationally  
509 expensive. Here, we use the 2-m simulations (i.e.,  $S_{2m}$  and  $S_{E2m}$ ) simulations as benchmarks for  
510 this assessment. That is,  $S_{2m}$  and  $S_{E2m}$  simulated variables are treated as the “truth” for  
511 “observed” and “elevated” river stage scenarios, and outputs from other simulations are  
512 compared to them to verify their performance. In the previous section, we showed that simulated  
513 water table levels from the model were virtually identical to observations. In this section, we  
514 further quantify biases of other variables of interest from the high-fidelity 2-m simulations.

515 The domain-averaged daily surface energy fluxes from  $S_{2m}$  show clear seasonal patterns,  
516 which are consistent in terms of their magnitudes and timing, reflecting mean climate conditions  
517 at the site (Figure S10). Driven by elevated river stages, latent heat from  $S_{E2m}$  is consistently  
518 higher than that from  $S_{2m}$ . The mean latent heat and sensible heat fluxes simulated by  $S_{2m}$  were  
519  $14.1 \text{ W m}^{-2}$  and  $38.7 \text{ W m}^{-2}$  over this period, compared to by  $18.50 \text{ W m}^{-2}$  and  $35.75 \text{ W m}^{-2}$  in  
520  $S_{E2m}$ . Figure 12 shows deviations of simulated LH and SH in the 20-m and 10-m simulations  
521 from the corresponding 2-m simulations. The deviations of both LH and SH were small across  
522 all the simulations driven by the observed river stage when surface and subsurface were  
523 decoupled. In the elevated simulations (i.e.,  $S_{E10m}$  and  $S_{E20m}$ ) when surface and subsurface

524 processes are more tightly coupled, errors in surface fluxes became significant in the coarse  
525 resolution simulations when compared to  $S_{E2m}$ . For example, the relative errors in LH were  
526 2.41% and 1.35% for  $S_{20m}$  and  $S_{10m}$ , respectively, as compared to  $S_{2m}$ , but grew as large as  
527 33.84% and 33.19% for  $S_{E20m}$  and  $S_{E10m}$ , respectively, when compared to  $S_{E2m}$ . The 10-m  
528 simulations outperformed the 20-m simulations under both scenarios but the magnitudes of  
529 errors were comparable. On the other hand, notably the vertical only simulation ( $S_{v2m}$ ) has a  
530 small error of 5.67% in LH compared to  $S_{2m}$ , indicating that lateral flow is less important when  
531 water table is deep.

532 To better understand how water in the river and the aquifer was connected, we also  
533 quantified the biases of subsurface state variables and fluxes including total water mass and  
534 tracer amount, as well as exchange rates of water and tracer at four boundaries of the subsurface  
535 domain using a similar approach (Figure S11 and Figure 13). Compared to the magnitude of total  
536 water mass in the domain (averaged  $919.45 \times 10^6$  Kg and  $1020.19 \times 10^6$  Kg in  $S_{2m}$  and  $S_{E2m}$ ),  
537 errors introduced by coarsening the resolution were very small under the observed river stage  
538 condition (0.04% for  $S_{20m}$  and 0.03% for  $S_{10m}$ ) and grew to 9.85% for  $S_{E20m}$  and 9.87% for  $S_{E10m}$   
539 in terms of total water mass in the domain (Table 5). However, for total tracer in the domain  
540 (averaged  $142.07 \times 10^6$  mol and  $172.46 \times 10^6$  mol in  $S_{2m}$  and  $S_{E2m}$ ) as a result of transport of river  
541 water in lateral and normal directions to the river, resolution clearly makes a difference under  
542 both observed condition and elevated scenarios (relative errors of 5.44% for  $S_{10m}$ , 10.40% for  
543  $S_{20m}$ , and 22.0% for both  $S_{E10m}$  and  $S_{E20m}$ ). The magnitude of computed mass exchange rates at  
544 the four boundaries (Figure S11) indicates that a coarse resolution promotes larger river water  
545 fluxes and groundwater exchanges, especially during the period of spring river stage increase  
546 under the elevated scenario. This forcing contributes to a significant bias in total tracer amount  
547 by the end of the simulation. The exchange rates at the other three boundaries follow the same  
548 pattern but with smaller magnitudes, especially for the west boundary that requires a significant  
549 gradient high enough to push river water further inland.

550 The results of simulations at three different resolutions indicated that: (1) the partitioning of  
551 the land surface energy budget is mainly controlled by near-surface moisture. Spatial resolution  
552 did not seem to be a significant factor in the computation of surface energy fluxes when the  
553 water table was deep at the semi-arid site; (2) if the surface and subsurface are tightly coupled as  
554 in the elevated river stage simulations, resolution becomes an important factor to consider for

555 credible simulations of the surface fluxes, as the land surface, subsurface, and riverine processes  
556 are expected to be more connected and coupled; (3) regardless of whether a tight coupling  
557 between the surface and subsurface occurs, if mass exchange rates and associated  
558 biogeochemical reactions in the aquifer are of interest, a higher resolution is desired close to the  
559 river shoreline to minimize terrain errors.

560

## 561 **5 Discussion and future work**

562 A coupled three-dimensional surface and subsurface land model was developed and applied to a  
563 site along the Columbia River to simulate interactions among river water, groundwater, and land  
564 surface processes. The model features the coupling of the open-source and state-of-the-art  
565 models portable on HPCs, the multi-physics reactive transport model PFLOTRAN and the  
566 CLM4.5. Both models are under active development and testing by their respective communities,  
567 therefore the coupled model could be updated to newer versions of PFLOTRAN and/or CLM to  
568 facilitate transfer of knowledge in a seamless fashion. The coupled model represents a new  
569 addition to the integrated surface and subsurface suite of models.

570 By applying the coupled model to a field site along the Columbia River shoreline driven by  
571 highly dynamic river boundary conditions resulting from upstream dam operations, we  
572 demonstrated that the model can be used to advance mechanistic understanding of stream-  
573 aquifer-land interactions surrounding near-shore alluvial aquifers that experience pressure  
574 changes induced by river stage variations along managed river reaches, which are of global  
575 significance as a result of over 30,000 dams constructed worldwide during the past half century.  
576 The land surface, subsurface, and riverine processes along such managed river corridors are  
577 expected to be more strongly coupled under projected hydro-climatic regimes as a result of  
578 increases in winter precipitation and early snowmelt. The dataset presented in this study can  
579 serve as a good benchmarking case for testing other coupled models for their applications to such  
580 systems. More data needs to be collected to facilitate the application and validation of the model  
581 to a larger domain for understanding the contribution of near-shore hydrologic exchange to water  
582 retention, biogeochemical cycling, and ecosystem functions along the river corridors.

583 By benchmarking the coarser resolution simulations at 20 m and 10 m against the 2-m  
584 simulations, we find that resolution is not a significant factor for surface flux simulations when

585 the water table is deep. However, resolution becomes important when the surface and subsurface  
586 processes are tightly coupled, and for accurately estimating the rate of mass exchange at the  
587 riverine boundaries, which can affect the calculation of biogeochemical processes involved in  
588 carbon and nitrogen cycles.

589 Our numerical experiments suggested that riverine, land surface, and subsurface processes  
590 could become more tightly coupled through two mechanisms in the near-shore environments: (1)  
591 expanding the periodically inundated fraction of the riparian zone and (2) enhancing moisture  
592 availability in the vadose zone in the inland domain through capillary rise. Both mechanisms can  
593 lead to increases in vadose-zone moisture availability and higher evapotranspiration rates. The  
594 latter is critical for understanding ecosystem functioning, biogeochemical cycling, and land-  
595 atmosphere interactions along river corridors in arid and semi-arid regions that are expected to  
596 experience new hydro-climatic regimes in a changing climate. However, these systems have  
597 been poorly accounted for in current-generation Earth system models and therefore require more  
598 attention in future studies.

599 We acknowledge that there are a number of limitations of this study that need to be addressed  
600 in future studies:

601 (1) Motivated by understanding the stream-aquifer-land interactions with a focus on  
602 groundwater and river water interactions along a river corridor situated in a semi-arid climate,  
603 the river boundary conditions were prescribed using observations with gaps filled by a 1-D  
604 hydrodynamics model. Future versions of the CP model need to incorporate two-way  
605 interactions between stream and aquifer by developing a surface flow component and testing the  
606 new implementation against standard benchmark cases [Kollet *et al.*, 2017; Maxwell *et al.*,  
607 2014].

608 (2) We note that CLM estimates the surface heat and moisture fluxes using the Monin-  
609 Obukhov Similarity Theory (section 2.1), which is only valid when the surface layer depth  $z \gg z_0$ ,  
610 where  $z_0$  is the aerodynamic roughness length. As reviewed by Basu and Lacser [2017], it is  
611 highly recommended that  $z > 50z_0$ , which should be proportional to the horizontal grid spacing to  
612 guarantee the validity of the Monin-Obukhov Similarity Theory [Arnqvist and Bergström, 2015].  
613 In our simulations, the majority of the Hanford 300A domain is covered by bare soil ( $z_0 = 0.01$   
614 m), grass ( $z_0 = 0.013$  m), shrubs ( $z_0 = 0.026-0.043$  m), and riparian trees (varies across the

615 seasons,  $z_0 = 0.008$  m when LAI = 2 in the summer and  $z_0 = 1.4$  when LAI = 0 in the winter).  
616 Therefore, a 2-m resolution is sufficiently coarse under most conditions except for the grid cells  
617 covered by riparian trees in the winter. Nevertheless, the wintertime latent heat and sensible heat  
618 fluxes are nearly zero due to extremely low energy inputs. Therefore, the 2-m simulations  
619 supported by the dense groundwater monitoring network at the site provide a valid benchmark  
620 for the coarser resolution simulations. For future applications of the coupled model, caution  
621 should be taken to evaluate the site condition for the validity of model parameterizations.

622 (3) We used the simulated surface energy fluxes from  $S_{2m}$  to verify coarser-resolution  
623 simulations. The simulated surface energy flux needs to be validated against eddy covariance  
624 tower observations, which are not available yet at the site. Nevertheless, we have made initial  
625 efforts to install eddy covariance systems at the site (see description in section 3.1 of *Gao et al.*  
626 [2017]) but the processing the flux data is still preliminary. We will report flux observations and  
627 validations of the surface energy budget simulations in future studies.

628 (4) Even when observed fluxes are available for validation, the model structural problems  
629 associated with ET parameterizations in CLM4.5 need to be addressed for reasonable  
630 simulations of the ET components, especially for the study site. That is, it has been well-  
631 documented that ET simulated by CLM4.5 and CLM4 could be enhanced when vegetation is  
632 removed. This ET enhancement over bare soil has been documented as a counter-intuitive bias  
633 for most unsaturated soils in CLM4 and CLM4.5 simulations [*Lawrence et al.*, 2012; *Tang and*  
634 *Riley*, 2013a]. *Tang and Riley* [2013a] explored a few potential causes for this likely bias (e.g.,  
635 soil resistance, litter layer resistance, and numerical time step). They found the implementation  
636 of a physically based soil resistance lowered the bias slightly, but concluded that the bias  
637 remained [*Tang and Riley*, 2013b]. Meanwhile, in studying ET over semiarid regions, *Swenson*  
638 *and Lawrence* [2014] proposed another soil resistance formulation to fix this excessive soil  
639 evaporation problem within CLM4.5. While their modification improved the simulated terrestrial  
640 water storage anomaly and ET when compared to GRACE data and FLUXNET-MTE data,  
641 respectively, the empirical nature of the soil resistance proposed could have underestimated the  
642 soil resistance variability when compared to other estimates [*Tang and Riley*, 2013b].

643

644 **Code availability**

645 CLM4.5 is an open-source software released as part of the Community Earth System Model  
646 (CESM) version 1.2 (<http://www.cesm.ucar.edu/models/cesm1.2>). The version of CLM4.5 used  
647 in CP v1.0 is a branch from the CLM developer's repository. Its functionality is scientifically  
648 consistent with descriptions in *Oleson et al.* [2013] with source codes refactored for a modular  
649 code design. Additional minor code modifications were added by the authors to support coupling  
650 with PFLOTRAN. Permission from the CESM Land Model Working Group has been obtained  
651 to release this CLM4.5 development branch but the National Center for Atmospheric Research  
652 cannot provide technical support for this version of the code CP v1.0. PFLOTRAN is an open-  
653 source software distributed under the terms of the GNU Lesser General Public License as  
654 published by the Free Software Foundation either version 2.1 of the License, or any later version.  
655 The CP v1.0 has two separate, open-source repositories for CLM4.5 and PFLOTRAN at:

- 656 • [https://bitbucket.org/clm\\_pflotran/clm-pflotran-trunk](https://bitbucket.org/clm_pflotran/clm-pflotran-trunk)
- 657 • [https://bitbucket.org/clm\\_pflotran/pflotran-clm-trunk](https://bitbucket.org/clm_pflotran/pflotran-clm-trunk)

658 The README guide for the CP v1.0 and dataset used in this study are available from the open-  
659 source repository [https://bitbucket.org/pnnl\\_sbr\\_sfa/notes-for-gmd-2017-35](https://bitbucket.org/pnnl_sbr_sfa/notes-for-gmd-2017-35).

660

661 **Acknowledgement**

662 This research was supported by the U.S. Department of Energy (DOE), Office of Biological and  
663 Environmental Research (BER), as part of BER's Subsurface Biogeochemical Research Program  
664 (SBR). This contribution originates from the SBR Scientific Focus Area (SFA) at the Pacific  
665 Northwest National Laboratory (PNNL).

666

667 **References**

- 668 Arnqvist, J., and Bergström, H. (2015), Flux-profile relation with roughness sublayer correction,  
669 *Quarterly Journal of the Royal Meteorological Society*, 141, 1191-1197, 10.1002/qj.2426, 2015.
- 670 Balay, S., J. Brown, K. Buschelman, V. Eijkhout, W. D. Gropp, D. Kaushik, M. G. Knepley, L.  
671 C. McInnes, B. F. Smith, and H. Zhang (2015), PETSc Users Manual, Tech. Rep. ANL-95/11—  
672 Revision 3.5*Rep.*, Argonne, Ill.
- 673 Basu, S., and Lacser, A. (2017). A Cautionary Note on the Use of Monin–Obukhov Similarity  
674 Theory in Very High-Resolution Large-Eddy Simulations, *Boundary-Layer Meteorology*, 163,  
675 351-355, 10.1007/s10546-016-0225-y.
- 676 Beven, K. J., and M. J. Kirkby (1979), A physically based, variable contributing area model of  
677 basin hydrology / Un modèle à base physique de zone d'appel variable de l'hydrologie du bassin  
678 versant, *Hydrological Sciences Bulletin*, 24(1), 43-69, doi:10.1080/02626667909491834.
- 679 Bjornstad, B. N. (2007), *On the Trail of the Ice Age Floods: A Geological Field Guide to the*  
680 *Mid-Columbian Basin*, KeoKee, Sandpoint, ID.
- 681 Burdine, N. T. (1953), Relative Permeability Calculations From Pore Size Distribution Data,  
682 doi:10.2118/225-G.
- 683 Chen, X., G. E. Hammond, C. J. Murray, M. L. Rockhold, V. R. Vermeul, and J. M. Zachara  
684 (2013), Application of ensemble-based data assimilation techniques for aquifer characterization  
685 using tracer data at Hanford 300 area, *Water Resources Research*, 49(10), 7064-7076,  
686 doi:10.1002/2012WR013285.
- 687 Chen, X., H. Murakami, M. S. Hahn, G. E. Hammond, M. L. Rockhold, J. M. Zachara, and Y.  
688 Rubin (2012), Three-dimensional Bayesian geostatistical aquifer characterization at the Hanford  
689 300 Area using tracer test data, *Water Resources Research*, 48(6), n/a-n/a,  
690 doi:10.1029/2011WR010675.
- 691 Clark, M. P., et al. (2015), Improving the representation of hydrologic processes in Earth System  
692 Models, *Water Resources Research*, 51(8), 5929-5956, doi:10.1002/2015WR017096.
- 693 Coleman, A., K. Larson, D. Ward, and J. Lettrick (2010), Development of a High-Resolution  
694 Bathymetry Dataset for the Columbia River through the Hanford Reach*Rep. PNNL-19878*,  
695 Pacific Northwest National Laboratory, Richland, WA.
- 696 Condon, L. E., R. M. Maxwell, and S. Gangopadhyay (2013), The impact of subsurface  
697 conceptualization on land energy fluxes, *Advances in Water Resources*, 60(0), 188-203,  
698 doi:http://dx.doi.org/10.1016/j.advwatres.2013.08.001.
- 699 Craig, A. P., M. Vertenstein, and R. Jacob (2012), A new flexible coupler for earth system  
700 modeling developed for CCSM4 and CESM1, *International Journal of High Performance*  
701 *Computing Applications*, 26(1), 31-42, doi:10.1177/1094342011428141.
- 702 Elsner, M. M., L. Cuo, N. Voisin, J. S. Deems, A. F. Hamlet, J. A. Vano, K. E. B. Mickelson, S.  
703 Y. Lee, and D. P. Lettenmaier (2010), Implications of 21st century climate change for the  
704 hydrology of Washington State, *Climatic Change*, 102(1-2), 225-260, doi:DOI 10.1007/s10584-  
705 010-9855-0.

706 Fan, Y., H. Li, and G. Miguez-Macho (2013), Global Patterns of Groundwater Table Depth,  
707 *Science*, 339(6122), 940-943.

708 Fan, Y., and G. Miguez-Macho (2011), A simple hydrologic framework for simulating wetlands  
709 in climate and earth system models, *Climate Dynamics*, 37(1), 253-278, doi:10.1007/s00382-  
710 010-0829-8.

711 Fischer, H., F. Kloep, S. Wilzcek, and M. T. Pusch (2005), A river's liver - microbial processes  
712 within the hyporheic zone of a large lowland river, *Biogeochemistry*, 76(2), 349-371.

713 Gaillardet, J., P. Regnier, R. Lauerwald, and P. Ciais (2014), Geochemistry of the Earth's surface  
714 GES-10 Paris France, 18-23 August, 2014. Carbon Leakage through the Terrestrial-  
715 aquatic Interface: Implications for the Anthropogenic CO<sub>2</sub> Budget, *Procedia Earth and  
716 Planetary Science*, 10, 319-324, doi:http://dx.doi.org/10.1016/j.proeps.2014.08.025.

717 Gao, Z., Russell, E. S., Missik, J. E. C., Huang, M., Chen, X., Strickland, C. E., Clayton, R.,  
718 Arntzen, E., Ma, Y., and Liu, H. (2017). A novel approach to evaluate soil heat flux calculation:  
719 An analytical review of nine methods, *Journal of Geophysical Research: Atmospheres*, n/a-n/a,  
720 10.1002/2017JD027160.

721 Gebler, S., Hendricks Franssen, H. J., Kollet, S. J., Qu, W., and Vereecken, H.: High resolution  
722 modelling of soil moisture patterns with TerrSysMP: A comparison with sensor network data,  
723 *Journal of Hydrology*, 547, 309-331, <https://doi.org/10.1016/j.jhydrol.2017.01.048>, 2017.

724 Gilbert, J. M., Maxwell, R. M., and Gochis, D. J.: Effects of Water-Table Configuration on the  
725 Planetary Boundary Layer over the San Joaquin River Watershed, California, *Journal of  
726 Hydrometeorology*, 18, 1471-1488, 10.1175/jhm-d-16-0134.1, 2017.

727 Hamlet, A. F., and D. P. Lettenmaier (1999), Effects of climate change on hydrology and water  
728 resources in the Columbia River basin, *Journal of the American Water Resources Association*,  
729 35(6), 1597-1623.

730 Hammond, G. E., and P. C. Lichtner (2010), Field-scale model for the natural attenuation of  
731 uranium at the Hanford 300 Area using high-performance computing, *Water Resources  
732 Research*, 46(9), n/a-n/a, doi:10.1029/2009WR008819.

733 Hammond, G. E., P. C. Lichtner, and R. T. Mills (2014), Evaluating the performance of parallel  
734 subsurface simulators: An illustrative example with PFLOTRAN, *Water Resources Research*,  
735 50(1), 208-228, doi:10.1002/2012WR013483.

736 Hammond, G. E., P. C. Lichtner, and M. L. Rockhold (2011), Stochastic simulation of uranium  
737 migration at the Hanford 300 Area, *Journal of Contaminant Hydrology*, 120-21, 115-128,  
738 doi:DOI 10.1016/j.jconhyd.2010.04.005.

739 Harvey, J., and M. Gooseff (2015), River corridor science: Hydrologic exchange and ecological  
740 consequences from bedforms to basins, *Water Resources Research*, 51(9), 6893-6922,  
741 doi:10.1002/2015WR017617.

742 Hauer, C., Siviglia, A., and Zolezzi, G.: Hydropeaking in regulated rivers – From process  
743 understanding to design of mitigation measures, *Science of The Total Environment*, 579, 22-26,  
744 <https://doi.org/10.1016/j.scitotenv.2016.11.028>, 2017.

745 Hou, Z., M. Huang, L. R. Leung, G. Lin, and D. M. Ricciuto (2012), Sensitivity of surface flux  
746 simulations to hydrologic parameters based on an uncertainty quantification framework applied

747 to the Community Land Model, *Journal of Geophysical Research: Atmospheres* (1984–2012),  
748 117(D15).

749 Hurrell, J. W., et al. (2013), The Community Earth System Model: A Framework for  
750 Collaborative Research, *Bulletin of the American Meteorological Society*, 94(9), 1339-1360,  
751 doi:10.1175/bams-d-12-00121.1.

752 Ji, X., C. Shen, and W. J. Riley (2015), Temporal evolution of soil moisture statistical fractal and  
753 controls by soil texture and regional groundwater flow, *Advances in Water Resources*, 86, Part  
754 A, 155-169, doi:http://dx.doi.org/10.1016/j.advwatres.2015.09.027.

755 Karra, S., Painter, S. L., and Lichtner, P. C. (2014). Three-phase numerical model for subsurface  
756 hydrology in permafrost-affected regions (PFLOTRAN-ICE v1.0), *The Cryosphere*, 8, 1935-  
757 1950, 10.5194/tc-8-1935-2014, 2014.

758 Keune, J., Gasper, F., Goergen, K., Hense, A., Shrestha, P., Sulis, M., and Kollet, S. (2016),  
759 Studying the influence of groundwater representations on land surface-atmosphere feedbacks  
760 during the European heat wave in 2003, *Journal of Geophysical Research: Atmospheres*, 121,  
761 13,301-313,325, 10.1002/2016JD025426, 2016.

762 Kollet, S. J., and R. M. Maxwell (2008), Capturing the influence of groundwater dynamics on  
763 land surface processes using an integrated, distributed watershed model, *Water Resources*  
764 *Research*, 44(2), n/a-n/a, doi:10.1029/2007WR006004.

765 Kollet, S., Sulis, M., Maxwell, R. M., Paniconi, C., Putti, M., Bertoldi, G., Coon, E. T., Cordano,  
766 E., Endrizzi, S., Kikinzon, E., Mouche, E., Mügler, C., Park, Y.-J., Refsgaard, J. C., Stisen, S.,  
767 and Sudicky, E. (2017).: The integrated hydrologic model intercomparison project, IH-MIP2: A  
768 second set of benchmark results to diagnose integrated hydrology and feedbacks, *Water*  
769 *Resources Research*, 53, 867-890, 10.1002/2016WR019191. Kumar, J., N. Collier, G. Bisht, R.  
770 T. Mills, P. E. Thornton, C. M. Iversen, and V. Romanovsky (2016), Modeling the  
771 spatiotemporal variability in subsurface thermal regimes across a low-relief polygonal tundra  
772 landscape, *The Cryosphere*, 10(5), 2241-2274, doi:10.5194/tc-10-2241-2016.

773 Lawrence, P. J., Feddema, J. J., Bonan, G. B., Meehl, G. A., O'Neill, B. C., Oleson, K. W.,  
774 Levis, S., Lawrence, D. M., Kluzek, E., Lindsay, K., and Thornton, P. E. (2012). Simulating the  
775 Biogeochemical and Biogeophysical Impacts of Transient Land Cover Change and Wood  
776 Harvest in the Community Climate System Model (CCSM4) from 1850 to 2100, *Journal of*  
777 *Climate*, 25, 3071-3095, 10.1175/jcli-d-11-00256.1. Lei, H., M. Huang, L. R. Leung, D. Yang, X.  
778 Shi, J. Mao, D. J. Hayes, C. R. Schwalm, Y. Wei, and S. Liu (2014), Sensitivity of global  
779 terrestrial gross primary production to hydrologic states simulated by the Community Land  
780 Model using two runoff parameterizations, *Journal of Advances in Modeling Earth Systems*,  
781 6(3), 658-679.

782 Leng, G., M. Huang, N. Voisin, X. Zhang, G. R. Asrar, and L. R. Leung (2016a), Emergence of  
783 new hydrologic regimes of surface water resources in the conterminous United States under  
784 future warming, *Environmental Research Letters*, 11(11), 114003.

785 Leng, G., X. Zhang, M. Huang, Q. Yang, R. Rafique, G. R. Asrar, and L. R. Leung (2016b),  
786 Simulating county-level crop yields in the conterminous United States using the community land  
787 model: The effects of optimizing irrigation and fertilization, *Journal of Advances in Modeling*  
788 *Earth Systems*, n/a-n/a, doi:10.1002/2016MS000645.

789 Leung, L. R., M. Huang, Y. Qian, and X. Liang (2011), Climate–soil–vegetation control on  
790 groundwater table dynamics and its feedbacks in a climate model, *Climate Dynamics*, 36(1), 57-  
791 81.

792 Lewis, J. M. (1995), The Story behind the Bowen Ratio, *Bulletin of the American*  
793 *Meteorological Society*, 76(12), 2433-2443, doi:10.1175/1520-  
794 0477(1995)076<2433:tsbtbr>2.0.co;2.

795 Liang, X., D. P. Lettenmaier, E. F. Wood, and S. J. Burges (1994), A simple hydrologically  
796 based model of land surface water and energy fluxes for general circulation models, *Journal of*  
797 *Geophysical Research: Atmospheres*, 99(D7), 14415-14428, doi:10.1029/94JD00483.

798 Lichtner, P. C., and G. E. Hammond (2012), Using High Performance Computing to Understand  
799 Roles of Labile and Nonlabile Uranium(VI) on Hanford 300 Area Plume Longevity, *Vadose*  
800 *Zone Journal*, 11(2), doi:10.2136/vzj2011.0097.

801 Lichtner, P. C., G. E. Hammond, C. Lu, S. Karra, G. Bisht, B. Andre, R. T. Mills, and K. Jitu  
802 (2015), PFLOTRAN User Manual: a Massively Parallel Reactive Flow and Transport Model for  
803 Describing Surface and Subsurface Processes *Rep.*

804 Liu, Y., G. Bisht, Z. M. Subin, W. J. Riley, and G. S. H. Pau (2016), A Hybrid Reduced-Order  
805 Model of Fine-Resolution Hydrologic Simulations at a Polygonal Tundra Site, *Vadose Zone*  
806 *Journal*, 15(2).

807 Maxwell, R. M., and L. E. Condon (2016), Connections between groundwater flow and  
808 transpiration partitioning, *Science*, 353(6297), 377-380, doi:10.1126/science.aaf7891.

809 Maxwell, R. M., L. E. Condon, and S. J. Kollet (2015), A high-resolution simulation of  
810 groundwater and surface water over most of the continental US with the integrated hydrologic  
811 model ParFlow v3, *Geosci. Model Dev.*, 8(3), 923-937, doi:10.5194/gmd-8-923-2015.

812 Maxwell, R. M., and S. J. Kollet (2008), Interdependence of groundwater dynamics and land-  
813 energy feedbacks under climate change, *Nature Geosci.*, 1(10), 665-669.

814 Maxwell, R. M., and N. L. Miller (2005), Development of a Coupled Land Surface and  
815 Groundwater Model, *Journal of Hydrometeorology*, 6(3), 233-247, doi:10.1175/JHM422.1.

816 Maxwell, R. M., et al. (2014), Surface-subsurface model intercomparison: A first set of  
817 benchmark results to diagnose integrated hydrology and feedbacks, *Water Resources Research*,  
818 50(2), 1531-1549, doi:10.1002/2013WR013725.

819 McNamara, J. P., D. Chandler, M. Seyfried, and S. Achet (2005), Soil moisture states, lateral  
820 flow, and streamflow generation in a semi-arid, snowmelt-driven catchment, *Hydrological*  
821 *Processes*, 19(20), 4023-4038, doi:10.1002/hyp.5869.

822 Miguez-Macho, G., and Y. Fan (2012), The role of groundwater in the Amazon water cycle: 1.  
823 Influence on seasonal streamflow, flooding and wetlands, *Journal of Geophysical Research:*  
824 *Atmospheres*, 117(D15), n/a-n/a, doi:10.1029/2012JD017539.

825 Nash, J. E., and J. V. Sutcliffe (1970), River flow forecasting through conceptual models part I  
826 — A discussion of principles, *Journal of Hydrology*, 10(3), 282-290,  
827 doi:http://dx.doi.org/10.1016/0022-1694(70)90255-6.

828 Nir, Y. K., L. Haibin, and F. Ying (2014), Groundwater flow across spatial scales: importance  
829 for climate modeling, *Environmental Research Letters*, 9(3), 034003.

830 Niu, G.-Y., C. Paniconi, P. A. Troch, R. L. Scott, M. Durcik, X. Zeng, T. Huxman, and D. C.  
831 Goodrich (2014), An integrated modelling framework of catchment-scale ecohydrological  
832 processes: 1. Model description and tests over an energy-limited watershed, *Ecohydrology*, 7(2),  
833 427-439, doi:10.1002/eco.1362.

834 Niu, G.-Y., Z.-L. Yang, R. E. Dickinson, and L. E. Gulden (2005), A simple TOPMODEL-based  
835 runoff parameterization (SIMTOP) for use in global climate models, *Journal of Geophysical*  
836 *Research: Atmospheres*, 110(D21), n/a-n/a, doi:10.1029/2005JD006111.

837 Niu, G.-Y., Z.-L. Yang, R. E. Dickinson, L. E. Gulden, and H. Su (2007), Development of a  
838 simple groundwater model for use in climate models and evaluation with Gravity Recovery and  
839 Climate Experiment data, *Journal of Geophysical Research: Atmospheres*, 112(D7), n/a-n/a,  
840 doi:10.1029/2006JD007522.

841 Oleson, K. W., et al. (2013), Technical Description of version 4.5 of the Community Land Model  
842 (CLM)Rep. Ncar Technical Note NCAR/TN-503+STR, National Center for Atmospheric  
843 Research, Boulder, CO.

844 Pau, G. S. H., G. Bisht, and W. J. Riley (2014), A reduced-order modeling approach to represent  
845 subgrid-scale hydrological dynamics for land-surface simulations: application in a polygonal  
846 tundra landscape, *Geosci. Model Dev.*, 7(5), 2091-2105, doi:10.5194/gmd-7-2091-2014.

847 Pau, G. S. H., C. Shen, W. J. Riley, and Y. Liu (2016), Accurate and efficient prediction of fine-  
848 resolution hydrologic and carbon dynamic simulations from coarse-resolution models, *Water*  
849 *Resources Research*, 52(2), 791-812, doi:10.1002/2015WR017782.

850 Rahman, M., M. Sulis, and S. J. Kollet (2015), The subsurface-land surface-atmosphere  
851 connection under convective conditions, *Advances in Water Resources*, 83, 240-249,  
852 doi:10.1016/j.advwatres.2015.06.003.

853 Rihani, J. F., F. K. Chow, and R. M. Maxwell (2015), Isolating effects of terrain and soil  
854 moisture heterogeneity on the atmospheric boundary layer: Idealized simulations to diagnose  
855 land-atmosphere feedbacks, *Journal of Advances in Modeling Earth Systems*, 7(2), 915-937,  
856 doi:10.1002/2014MS000371.

857 Riley, W. J., and C. Shen (2014), Characterizing coarse-resolution watershed soil moisture  
858 heterogeneity using fine-scale simulations, *Hydrol. Earth Syst. Sci.*, 18(7), 2463-2483,  
859 doi:10.5194/hess-18-2463-2014.

860 Sakaguchi, K., and Zeng, X.: Effects of soil wetness, plant litter, and under-canopy atmospheric  
861 stability on ground evaporation in the Community Land Model (CLM3.5), *Journal of*  
862 *Geophysical Research: Atmospheres*, 114, n/a-n/a, 10.1029/2008JD010834, 2009.

863 Schaller, M. F., and Y. Fan (2009), River basins as groundwater exporters and importers:  
864 Implications for water cycle and climate modeling, *Journal of Geophysical Research:*  
865 *Atmospheres*, 114(D4), n/a-n/a, doi:10.1029/2008JD010636.

866 Shen, C., J. Niu, and M. S. Phanikumar (2013), Evaluating controls on coupled hydrologic and  
867 vegetation dynamics in a humid continental climate watershed using a subsurface-land surface  
868 processes model, *Water Resources Research*, 49(5), 2552-2572, doi:10.1002/wrcr.20189.

869 Shen, C., W. J. Riley, K. M. Smithgall, J. M. Melack, and K. Fang (2016), The fan of influence  
870 of streams and channel feedbacks to simulated water and carbon fluxes, *Water Resources*  
871 *Research*, doi:10.1002/2015WR018086.

872 Shi, Y., K. J. Davis, C. J. Duffy, and X. Yu (2013), Development of a Coupled Land Surface  
873 Hydrologic Model and Evaluation at a Critical Zone Observatory, *Journal of Hydrometeorology*,  
874 *14*(5), 1401-1420, doi:10.1175/JHM-D-12-0145.1.

875 Shrestha, P., Sulis, M., Masbou, M., Kollet, S., and Simmer, C.: A Scale-Consistent Terrestrial  
876 Systems Modeling Platform Based on COSMO, CLM, and ParFlow, *Monthly Weather Review*,  
877 *142*, 3466-3483, 10.1175/mwr-d-14-00029.1, 2014.

878 Sulis, M., Williams, J. L., Shrestha, P., Diederich, M., Simmer, C., Kollet, S. J., and Maxwell, R.  
879 M.: Coupling Groundwater, Vegetation, and Atmospheric Processes: A Comparison of Two  
880 Integrated Models, *Journal of Hydrometeorology*, *18*, 1489-1511, 10.1175/jhm-d-16-0159.1,  
881 2017.

882 Swenson, S. C., and Lawrence, D. M.: Assessing a dry surface layer-based soil resistance  
883 parameterization for the Community Land Model using GRACE and FLUXNET-MTE data,  
884 *Journal of Geophysical Research: Atmospheres*, *119*, 10,299-210,312, 10.1002/2014JD022314,  
885 2014.

886 Tang, G., Yuan, F., Bisht, G., Hammond, G. E., Lichtner, P. C., Kumar, J., Mills, R. T., Xu, X.,  
887 Andre, B., Hoffman, F. M., Painter, S. L., and Thornton, P. E.: Addressing numerical challenges  
888 in introducing a reactive transport code into a land surface model: a biogeochemical modeling  
889 proof-of-concept with CLM-PFLOTRAN 1.0, *Geosci. Model Dev.*, *9*, 927-946, 10.5194/gmd-9-  
890 927-2016, 2016.

891 Tang, J., and Riley, W. J. (2013a) Impacts of a new bare-soil evaporation formulation on site,  
892 regional, and global surface energy and water budgets in CLM4, *Journal of Advances in*  
893 *Modeling Earth Systems*, *5*, 558-571, 10.1002/jame.20034, 2013a.

894 Tang, J. Y., and Riley, W. J. (2013b) A new top boundary condition for modeling surface  
895 diffusive exchange of a generic volatile tracer: theoretical analysis and application to soil  
896 evaporation, *Hydrol. Earth Syst. Sci.*, *17*, 873-893, 10.5194/hess-17-873-2013, 2013b.

897 Taylor, R. G., et al. (2013), Ground water and climate change, *Nature Clim. Change*, *3*(4), 322-  
898 329.

899 Thorne, P. D., M. P. Bergeron, M. D. Williams, and V. L. Freedman (2006), Groundwater Data  
900 Package for Hanford Assessments *Rep. PNNL-14753*, Pacific Northwest National Laboratory,  
901 Richland, WA.

902 Tiffan, K. F., R. D. Garland, and D. W. Rondorf (2002), Quantifying flow-dependent changes in  
903 subyearling fall chinook salmon rearing habitat using two-dimensional spatially explicit  
904 modeling, *North American Journal of Fisheries Management*, *22*(3), 713-726, doi:Doi  
905 10.1577/1548-8675(2002)022<0713:Qfdcis>2.0.Co;2.

906 van Genuchten, M. T. (1980), A Closed-form Equation for Predicting the Hydraulic  
907 Conductivity of Unsaturated Soils1, *Soil Science Society of America Journal*, *44*(5), 892-898,  
908 doi:10.2136/sssaj1980.03615995004400050002x.

909 Waichler, S. R., W. A. Perkins, and M. C. Richmond (2005), Hydrodynamic Simulation of the  
910 Columbia River, Hanford Reach, 1940-2004Rep. *PNNL-15226*, Pacific Northwest National  
911 Laboratory, Richland, WA.

912 Williams, M. D., M. L. Rockhold, P. D. Thorne, and Y. Chen (2008), Three-Dimensional  
913 Groundwater Models of the 300 Area at the Hanford Site, Washington StateRep. *PNNL-17708*,  
914 Pacific Northwest National Laboratory, Richland, WA.

915 Wood, E. F., D. P. Lettenmaier, and V. G. Zartarian (1992), A land-surface hydrology  
916 parameterization with subgrid variability for general circulation models, *Journal of Geophysical*  
917 *Research: Atmospheres*, 97(D3), 2717-2728, doi:10.1029/91JD01786.

918 Xu, X., et al. (2016), A multi-scale comparison of modeled and observed seasonal methane  
919 emissions in northern wetlands, *Biogeosciences*, 13(17), 5043-5056, doi:10.5194/bg-13-5043-  
920 2016.

921 Zachara, J. M., Chen, X., Murray, C., and Hammond, G. (2016). River stage influences on  
922 uranium transport in a hydrologically dynamic groundwater-surface water transition zone, *Water*  
923 *Resources Research*, 52, 1568-1590, 10.1002/2015WR018009, 2016.

924 Zeng, X., Zhao, M., and Dickinson, R. E. (1998), Intercomparison of bulk aerodynamic  
925 algorithms for the computation of sea surface fluxes using TOGA COARE and TAO data,  
926 *Journal of Climate*, 11, 2628-2644, 1998.

927 Zeng, X., Dickinson, R. E., Barlage, M., Dai, Y., Wang, G., and Oleson, K. (2005), Treatment of  
928 undercanopy turbulence in land models, *Journal of Climate*, 18, 5086-5094,  
929 10.1175/JCLI3595.1.

930 Zeng, X., and Wang, A. (2007), Consistent Parameterization of Roughness Length and  
931 Displacement Height for Sparse and Dense Canopies in Land Models, *Journal of*  
932 *Hydrometeorology*, 8, 730-737, 10.1175/jhm607.1.

933 Zeng, X., and Decker, M. (2009), Improving the Numerical Solution of Soil Moisture-Based  
934 Richards Equation for Land Models with a Deep or Shallow Water Table, *Journal of*  
935 *Hydrometeorology*, 10, 308-319, 10.1175/2008JHM1011.1.

936 Zhang, B., J. L. Tang, C. Gao, and H. Zepp (2011), Subsurface lateral flow from hillslope and its  
937 contribution to nitrate loading in streams through an agricultural catchment during subtropical  
938 rainstorm events, *Hydrol. Earth Syst. Sci.*, 15(10), 3153-3170, doi:10.5194/hess-15-3153-2011.

939 Zhou, T., B. Nijssen, H. L. Gao, and D. P. Lettenmaier (2016), The Contribution of Reservoirs to  
940 Global Land Surface Water Storage Variations, *Journal of Hydrometeorology*, 17(1), 309-325,  
941 doi:10.1175/jhm-d-15-0002.1.

942

943

944 **Tables and Figures**

945

946 Table 1. Summary of numerical experiments

<b>Experiments</b>	<b>Model</b>	<b>Horizontal Resolution</b>	<b>Lateral flow</b>	<b>River Stage (m)</b>
<b>S<sub>v2m</sub></b>	CP v1.0	2m	No	Observed
<b>S<sub>2m</sub></b>	CP v1.0	2m	Yes	Observed
<b>S<sub>10m</sub></b>	CP v1.0	10m	Yes	Observed
<b>S<sub>20m</sub></b>	CP v1.0	20m	Yes	Observed
<b>S<sub>E2m</sub></b>	CP v1.0	2m	Yes	Observed +5
<b>S<sub>E10m</sub></b>	CP v1.0	10m	Yes	Observed +5
<b>S<sub>E20m</sub></b>	CP v1.0	20m	Yes	Observed +5
<b>CLM<sub>2m</sub></b>	CLM4.5	2m	No	Not applicable

947

948

949 Table 2. Hydrogeological material properties of Hanford and Ringold materials.

Material	Porosity	Permeability (m <sup>2</sup> )	Van Genuchten/Burdine Parameters		
			Res. Sat.	m	alpha
<b>Hanford</b>	0.20	$7.387 \times 10^{-9}$	0.16	0.34	$7.27 \times 10^{-4}$
<b>Ringold</b>	0.40	$1.055 \times 10^{-12}$	0.13	0.75	$1.43 \times 10^{-4}$

950

951

952 Table 3. The comparison between simulated and observed water table levels

Well number	S <sub>2m</sub>		S <sub>10m</sub>		S <sub>20m</sub>	
	RMSE (m)	N-S	RMSE (m)	N-S	RMSE (m)	N-S
<b>399-3-29</b>	0.022	0.999	0.022	0.999	0.021	0.999
<b>399-3-34</b>	0.011	1.000	0.011	1.000	0.006	1.000
<b>399-2-01</b>	0.039	0.997	0.038	0.997	0.029	0.998
<b>399-1-60</b>	0.016	1.000	0.016	0.999	0.013	1.000
<b>399-2-33</b>	0.028	0.998	0.028	0.998	0.022	0.999
<b>399-1-21A</b>	0.023	0.999	0.023	0.999	0.020	0.999
<b>399-2-03</b>	0.037	0.997	0.037	0.997	0.029	0.998
<b>399-2-02</b>	0.045	0.995	0.045	0.995	0.042	0.996
<b>mean</b>	0.028	0.998	0.028	0.998	0.023	0.999

953

954

955 Table 4. The relative error in surface energy fluxes simulated by  $S_{10m}$  and  $S_{20m}$  benchmarked against  $S_{2m}$   
956 and by  $S_{E10m}$  and  $S_{E20m}$  benchmarked against  $S_{E2m}$

<b><i>Simulation</i></b>	<b><i>Latent heat flux (%)</i></b>	<b><i>Sensible heat flux (%)</i></b>
$S_{v2m}$	5.67	1.63
$S_{10m}$	1.35	0.78
$S_{20m}$	2.41	1.42
$S_{E10m}$	33.19	13.71
$S_{E20m}$	33.84	14.18

957

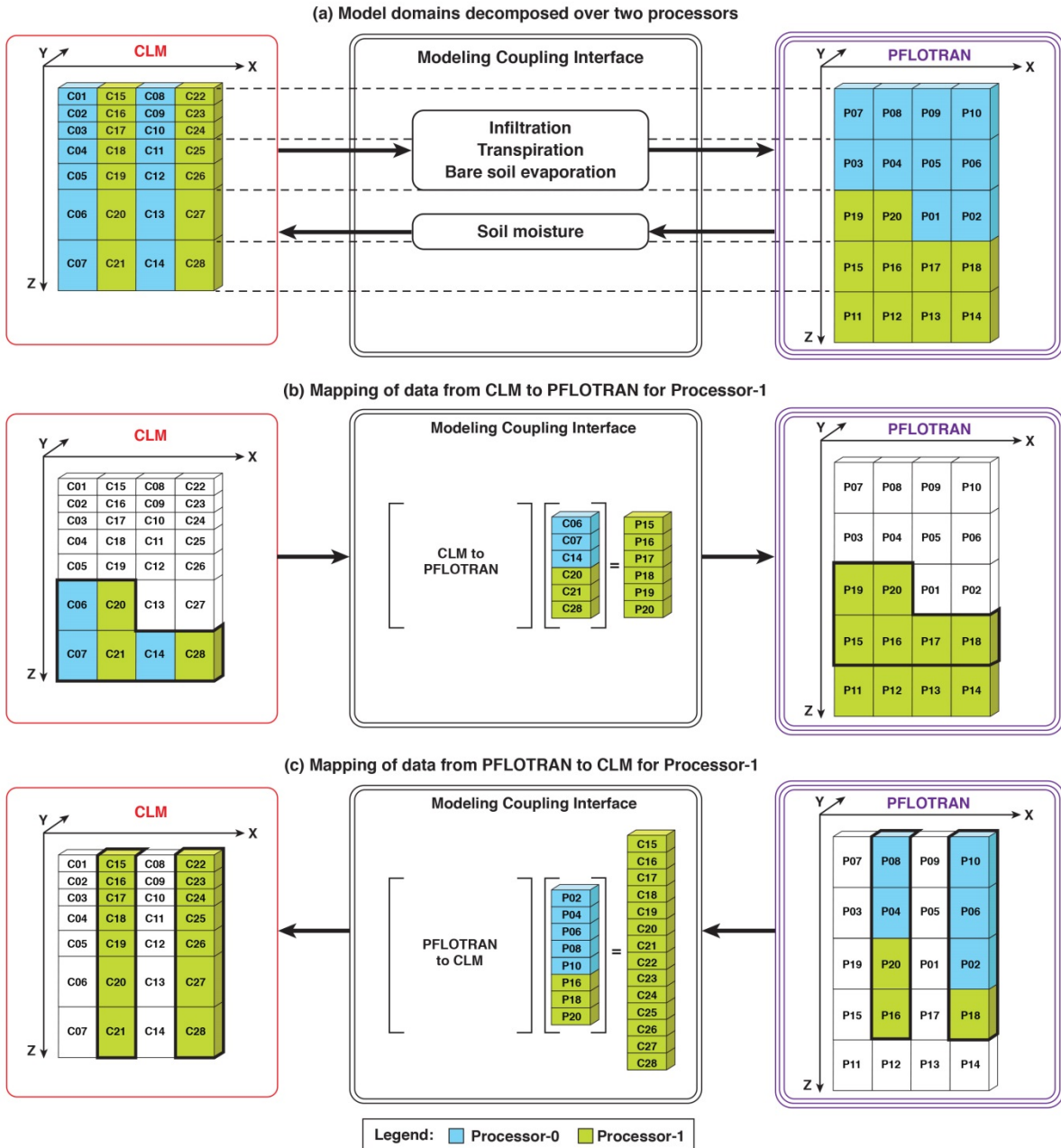
958

959 Table 5. The relative error in total water mass and tracer amount in the subsurface simulated in  $S_{10m}$  and  
960  $S_{20m}$  benchmarked against  $S_{2m}$  and by  $S_{E10m}$  and  $S_{E20m}$  benchmarked against  $S_{E2m}$

<b><i>Simulation</i></b>	Total water mass (%)	Total tracer (%)
<b><math>S_{10m}</math></b>	0.03	5.44
<b><math>S_{20m}</math></b>	0.04	10.40
<b><math>S_{E10m}</math></b>	9.87	22.00
<b><math>S_{E20m}</math></b>	9.85	22.00

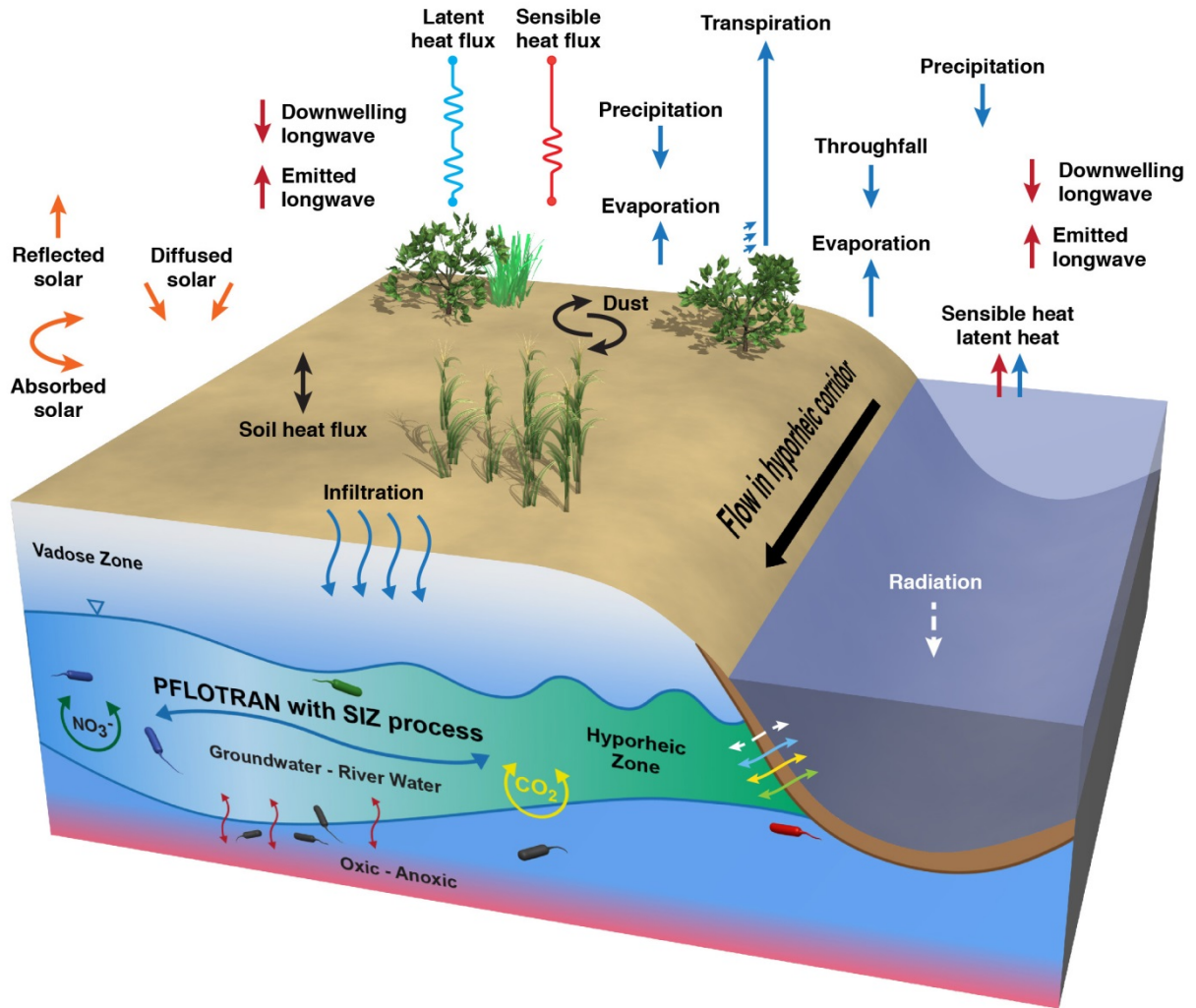
961

962

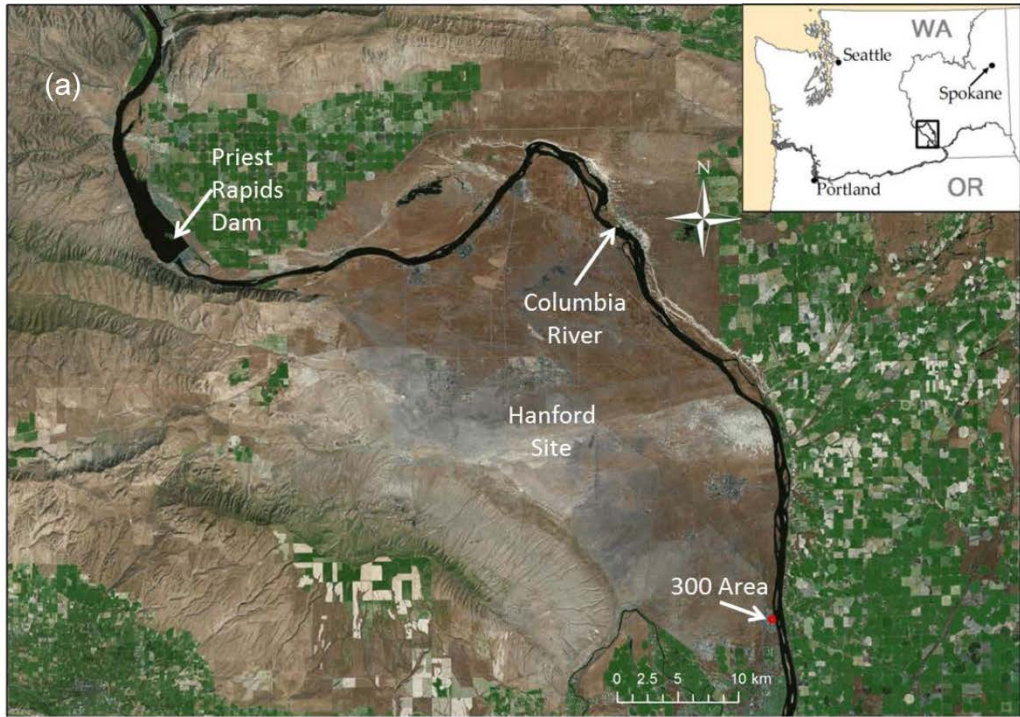


963  
 964 Figure 1. Schematic representations of the model coupling interface of CP v1.0. (a) Domain  
 965 decomposition of a hypothetical CLM and PFLOTRAN domain comprising of 4x1x7 and 4x1x5 grids in x,  
 966 y, and z directions across two processors as shown in blue and green. (b) Mapping of water fluxes from  
 967 CLM onto PFLOTRAN domain via a local sparse matrix vector product for grids on processor 1. (c)  
 968 Mapping of updated soil moisture from PFLOTRAN onto CLM domain via a local sparse matrix vector  
 969 product for grids on processor 1.

970

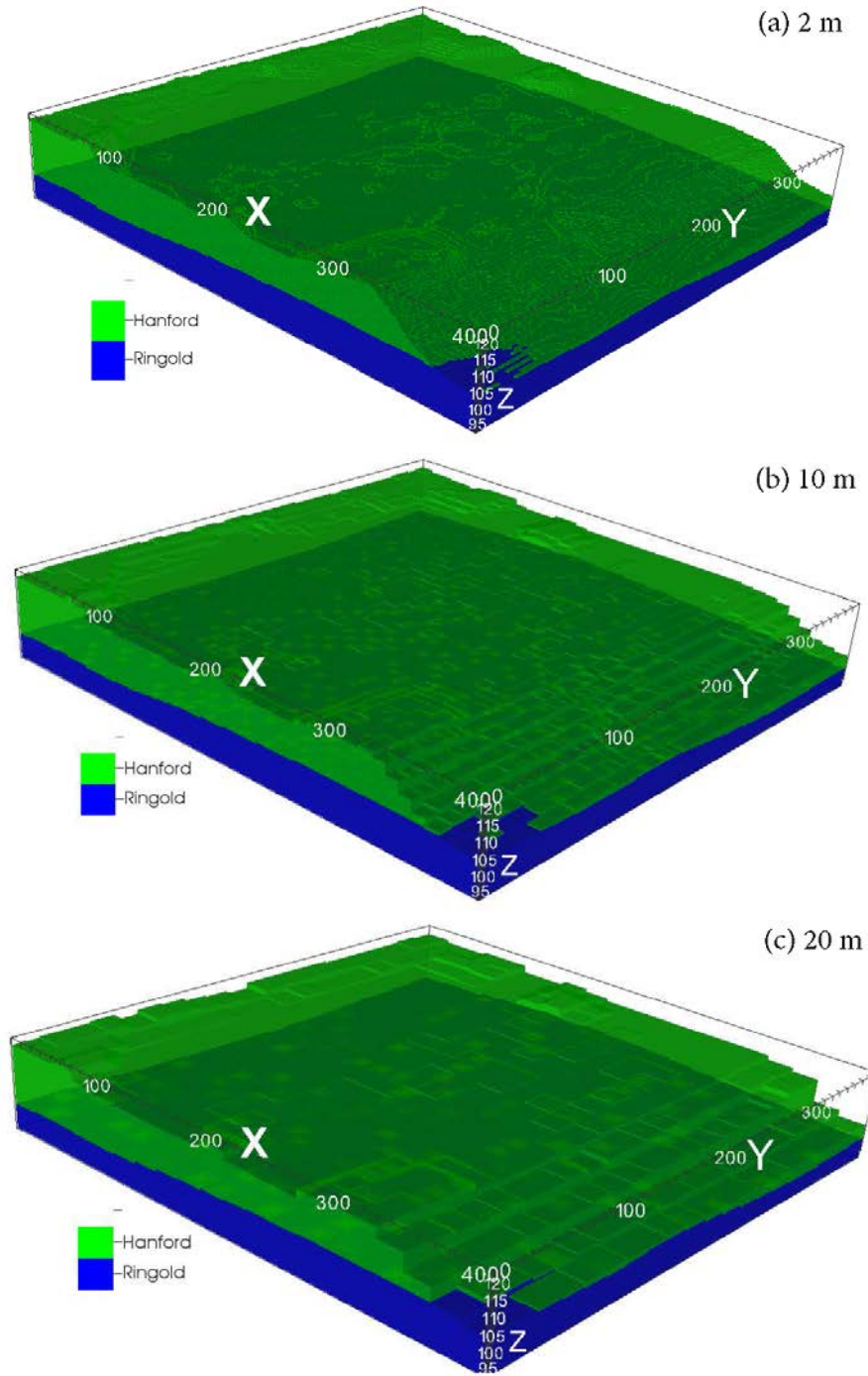


971 Figure 2. Schematic representation of hydrologic processes simulated in CP v1.0  
 972



973

974 Figure 3. (a) The Hanford Reach of the Columbia River and the Hanford Site location in south-central  
 975 Washington State, USA; (b) the 400 m x 400 m modeling domain located in the Hanford 300 Area.

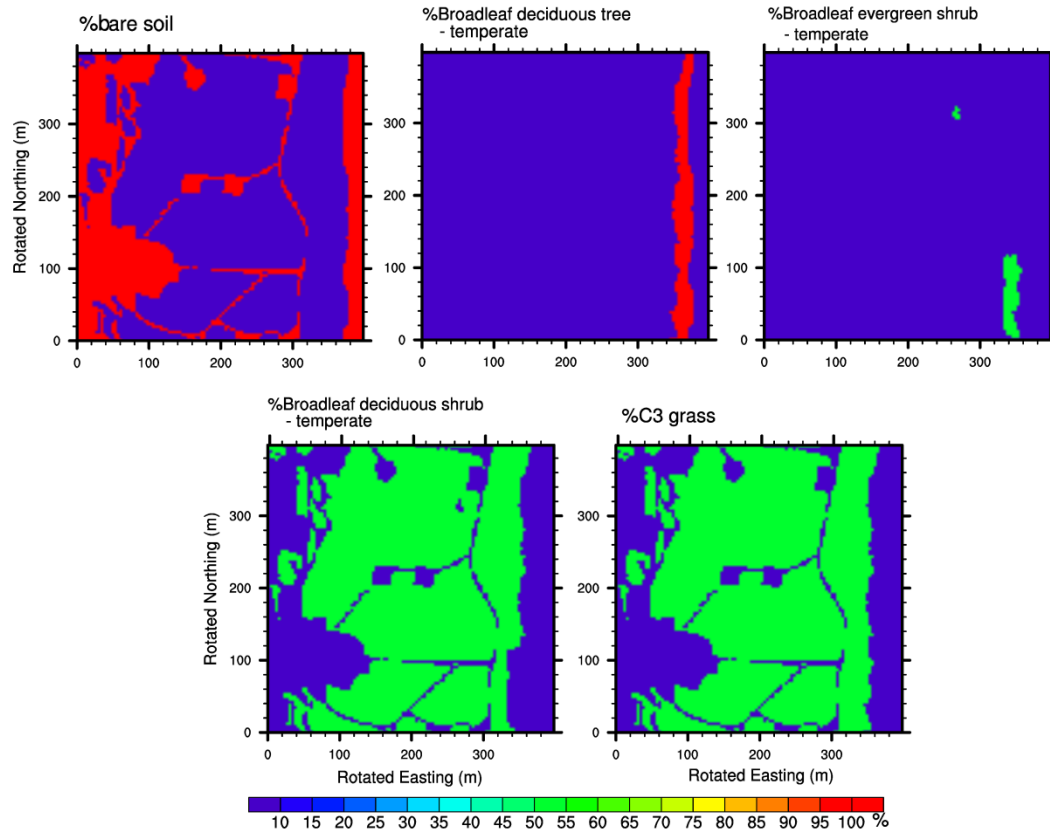


976

977 Figure 4. PFLOTRAN meshes and associated material IDs at (a) 2-m; (b) 10-m; and (c) 20-m resolutions

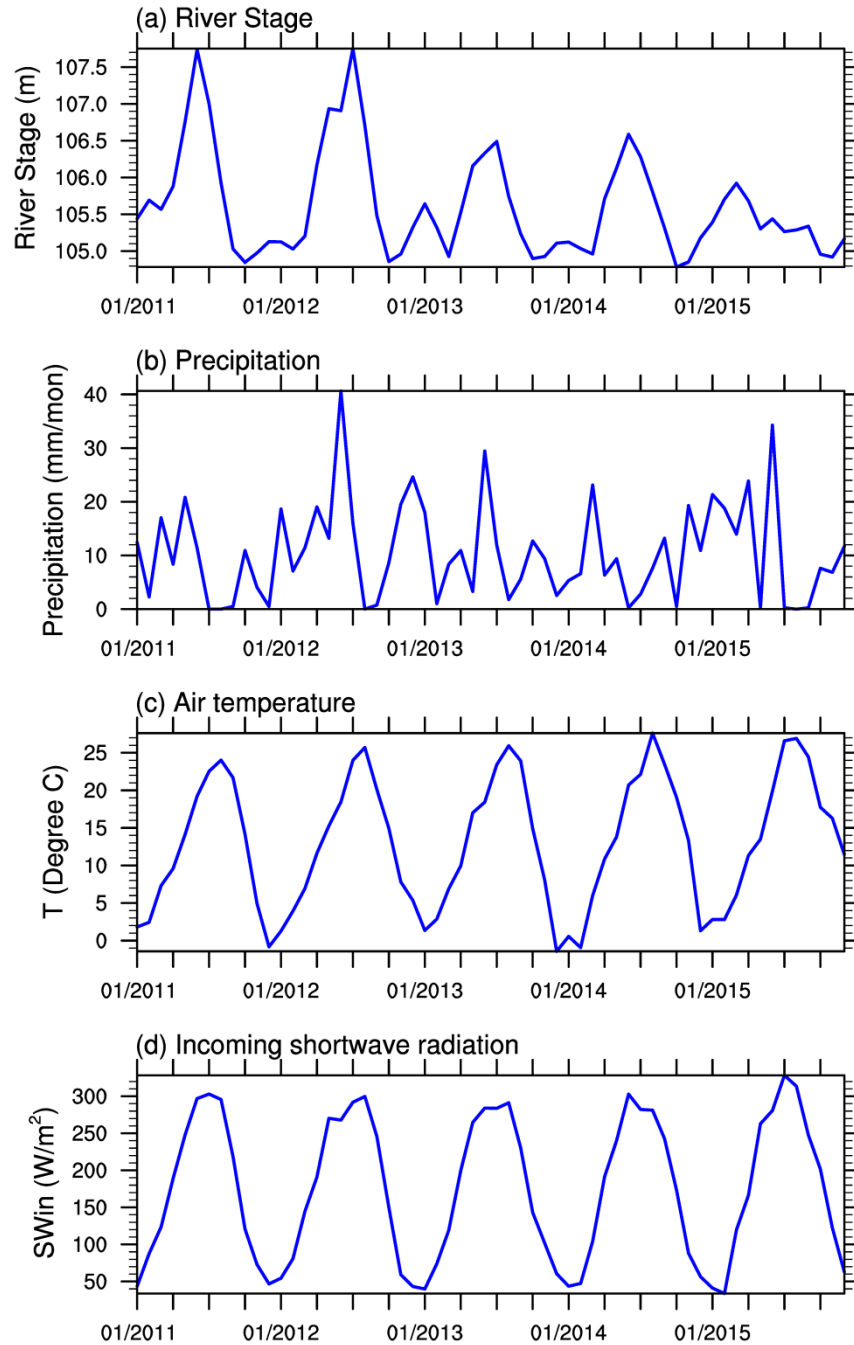
978

979



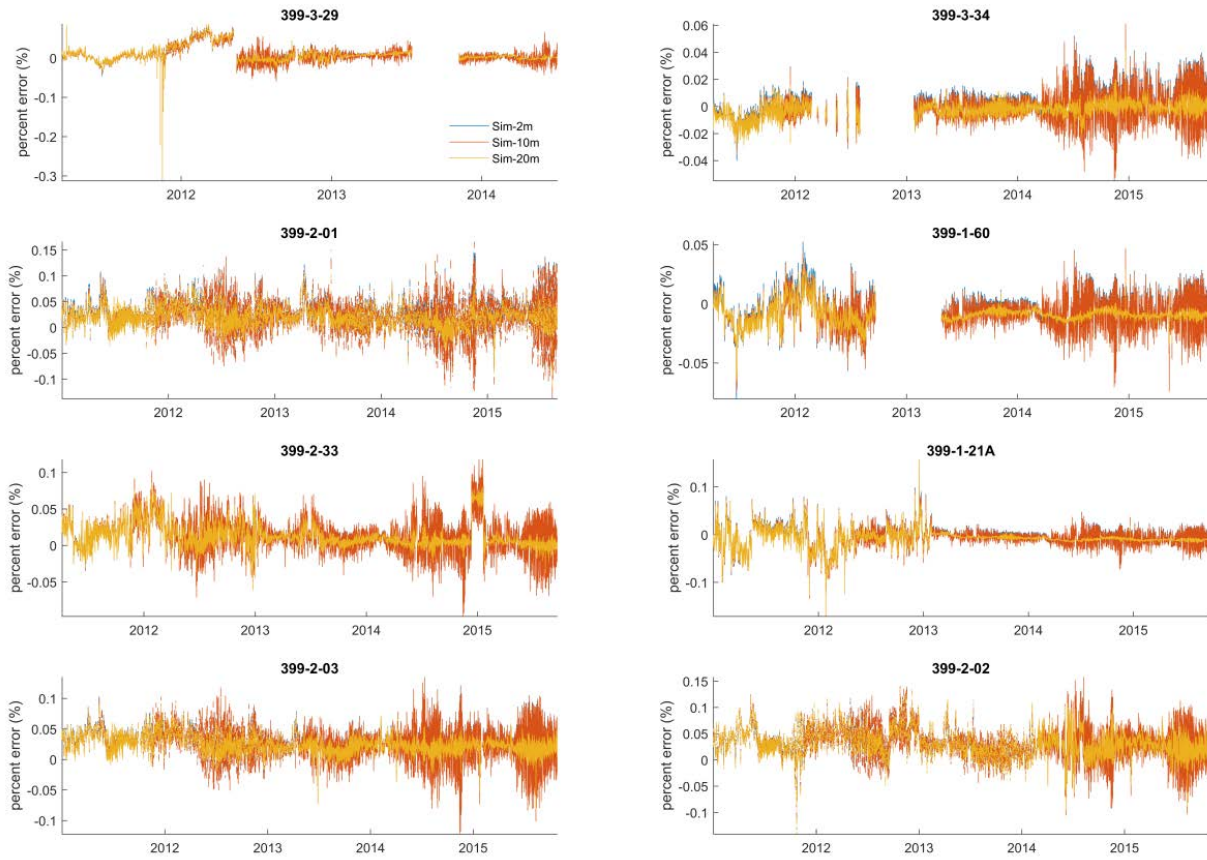
980

981 Figure 5. Plant function types at 2-m resolution as inputs for CLM4.5



982

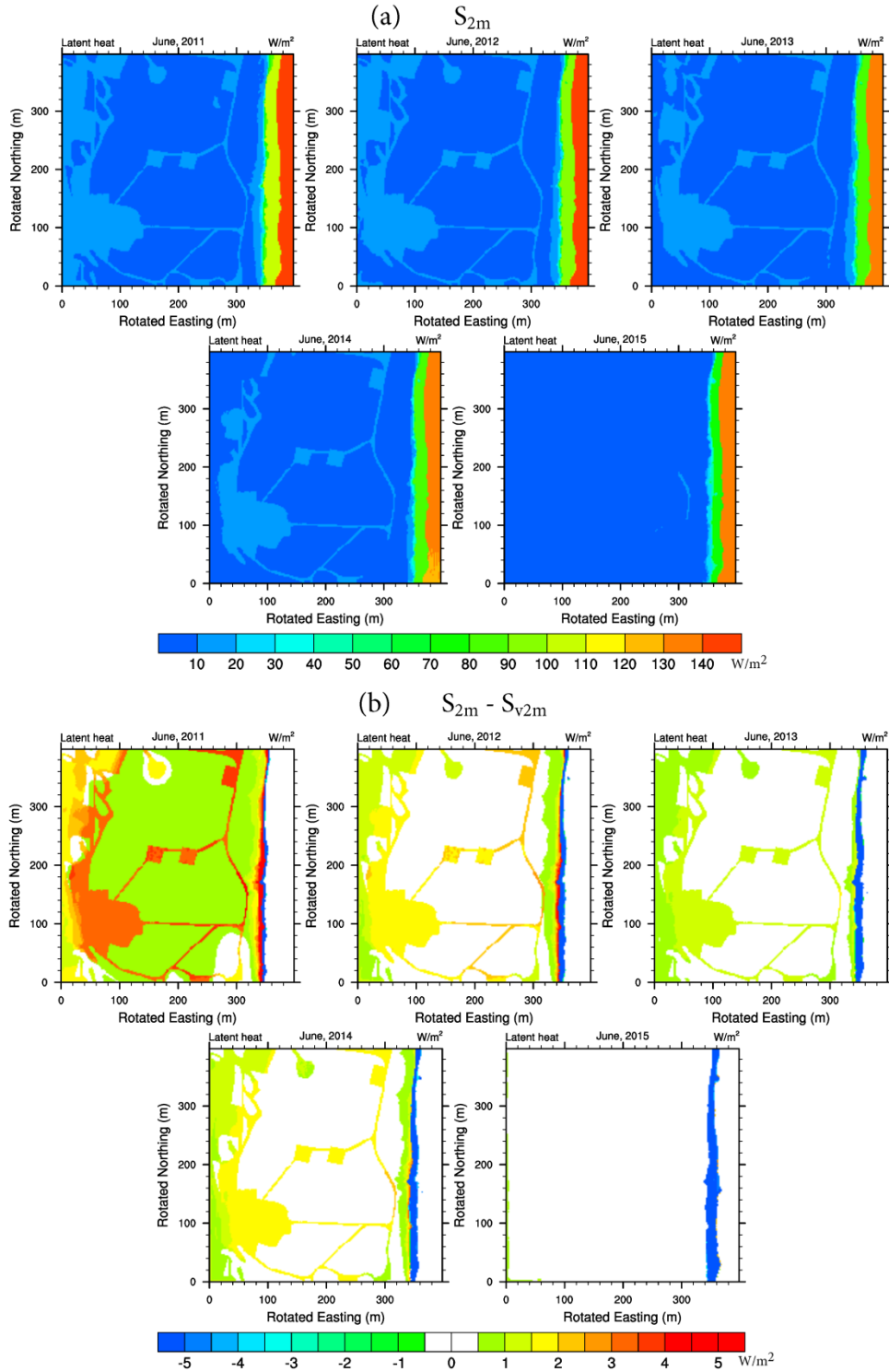
983 Figure 6. Hydro-meteorological drivers in the study period: (a) monthly mean river Stage; (b) monthly  
 984 total precipitation; (c) monthly mean surface air temperature; (d) and monthly mean incoming shortwave  
 985 radiation.



986

987 Figure 7. Deviation (in percentages) of simulated water table levels from observations at selected wells  
 988 shown in Figure 3b.

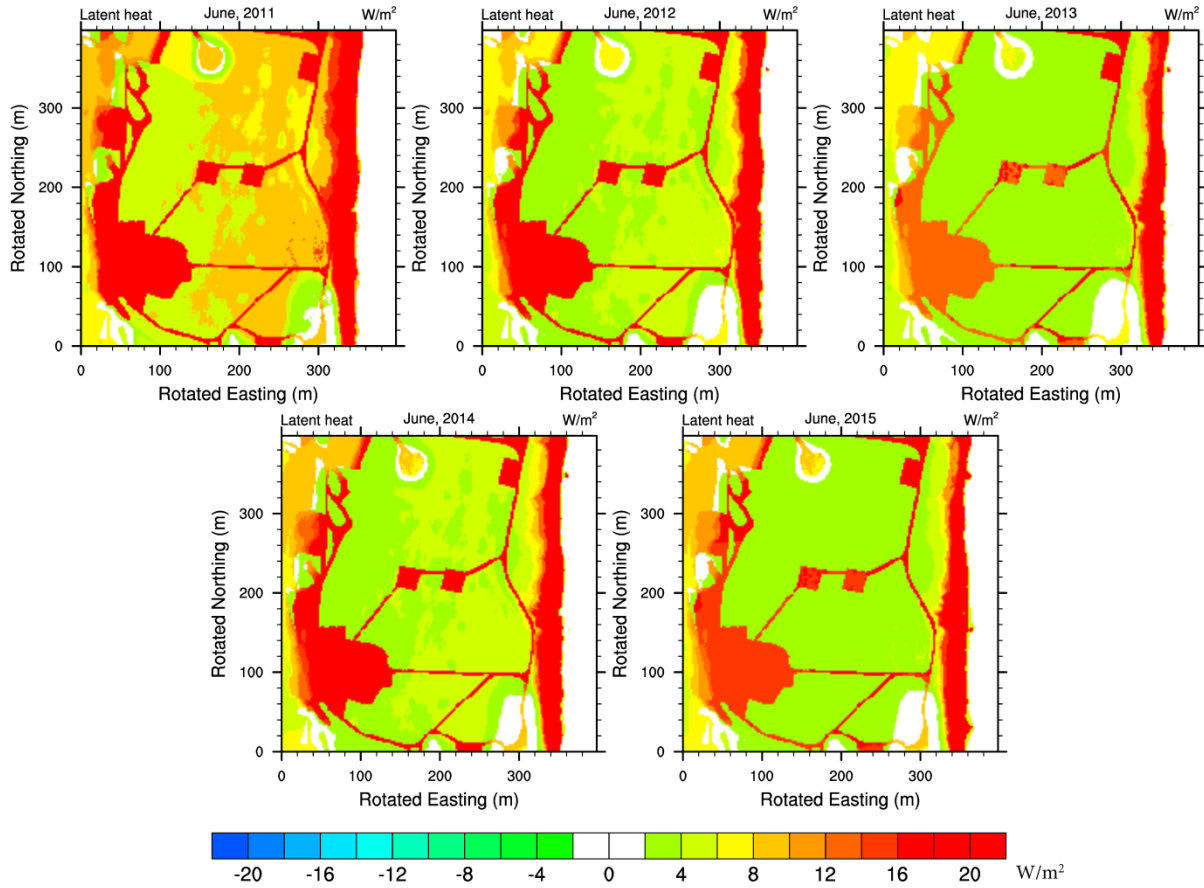
989



990

991 Figure 8. (a) Simulated latent heat fluxes in June from the 3-D simulation ( $S_{2m}$ ); and (b) the difference  
 992 between the 3-D and vertical only simulations (i.e.,  $S_{2m} - S_{v2m}$ ).

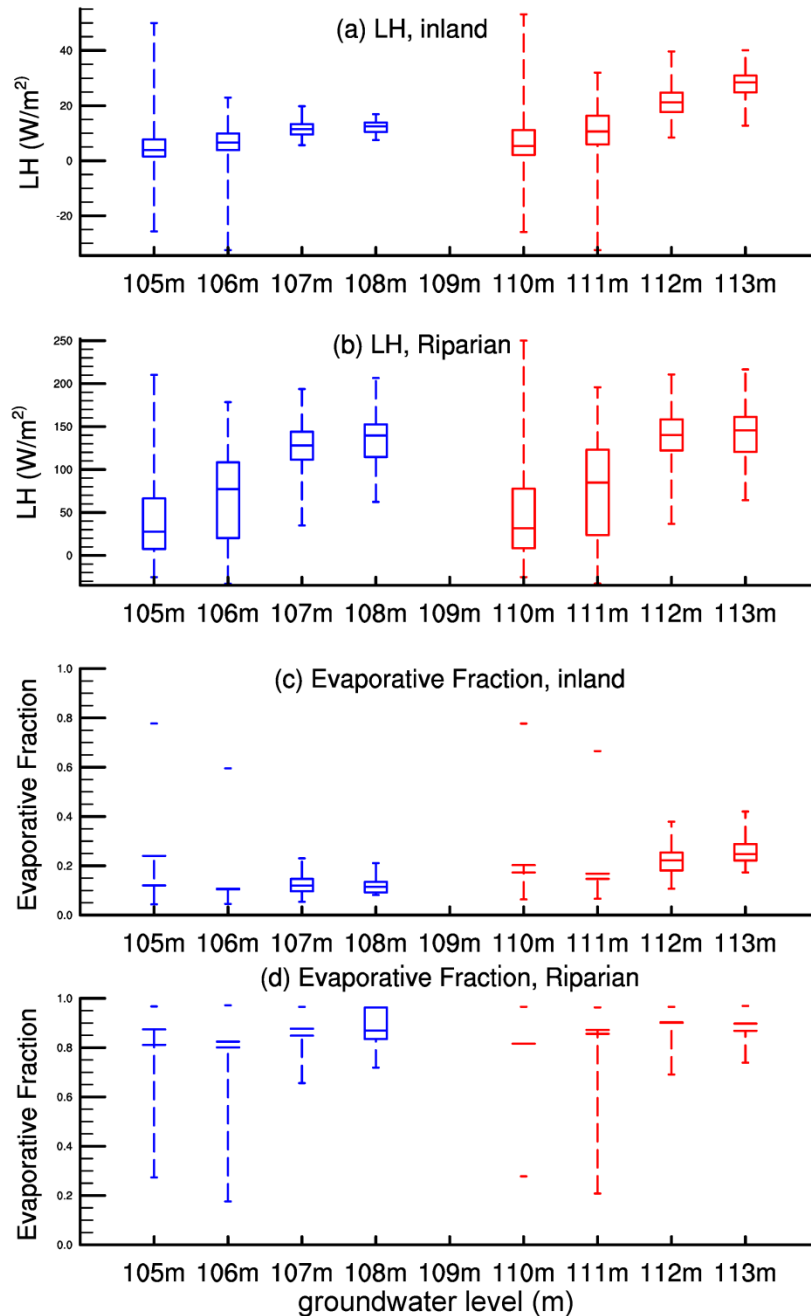
993



994

995 Figure 9. Difference between simulated latent heat fluxes by  $S_{E2m}$  and  $S_{2m}$  in June.

996



997

998

999

1000

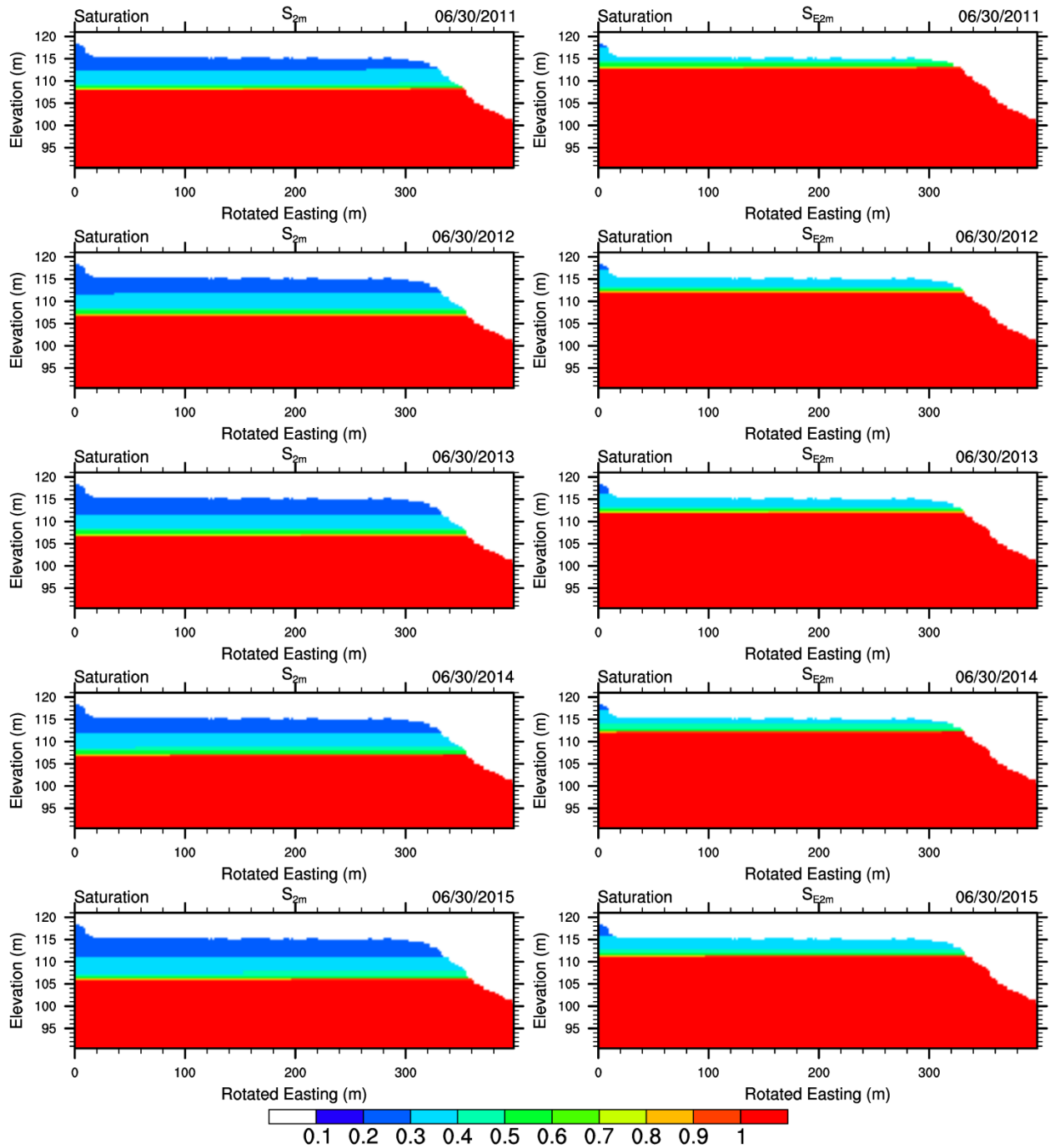
1001

1002

1003

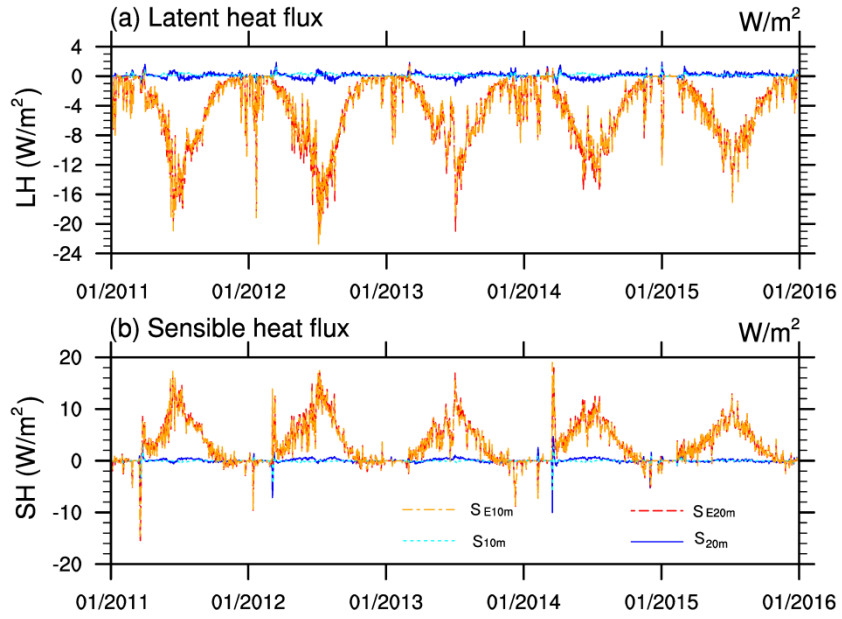
Figure 10. Boxplots of (a) land heat fluxes over the inland domain; (b) and latent heat fluxes in the riparian zone; (c) Evaporative fractions over the inland domain; (d) Evaporative fractions in the riparian zone in relation to groundwater table levels in the five-year period. The red boxes and whiskers represent summary statistics from  $S_{2m}$ , and red ones indicate those from  $S_{E2m}$ . The bottom and top of each box are the 25<sup>th</sup> and 75<sup>th</sup> percentile, the band inside the box is median, and the ends of the whiskers are maximum and minimum values, respectively.

### Transect, y=200m



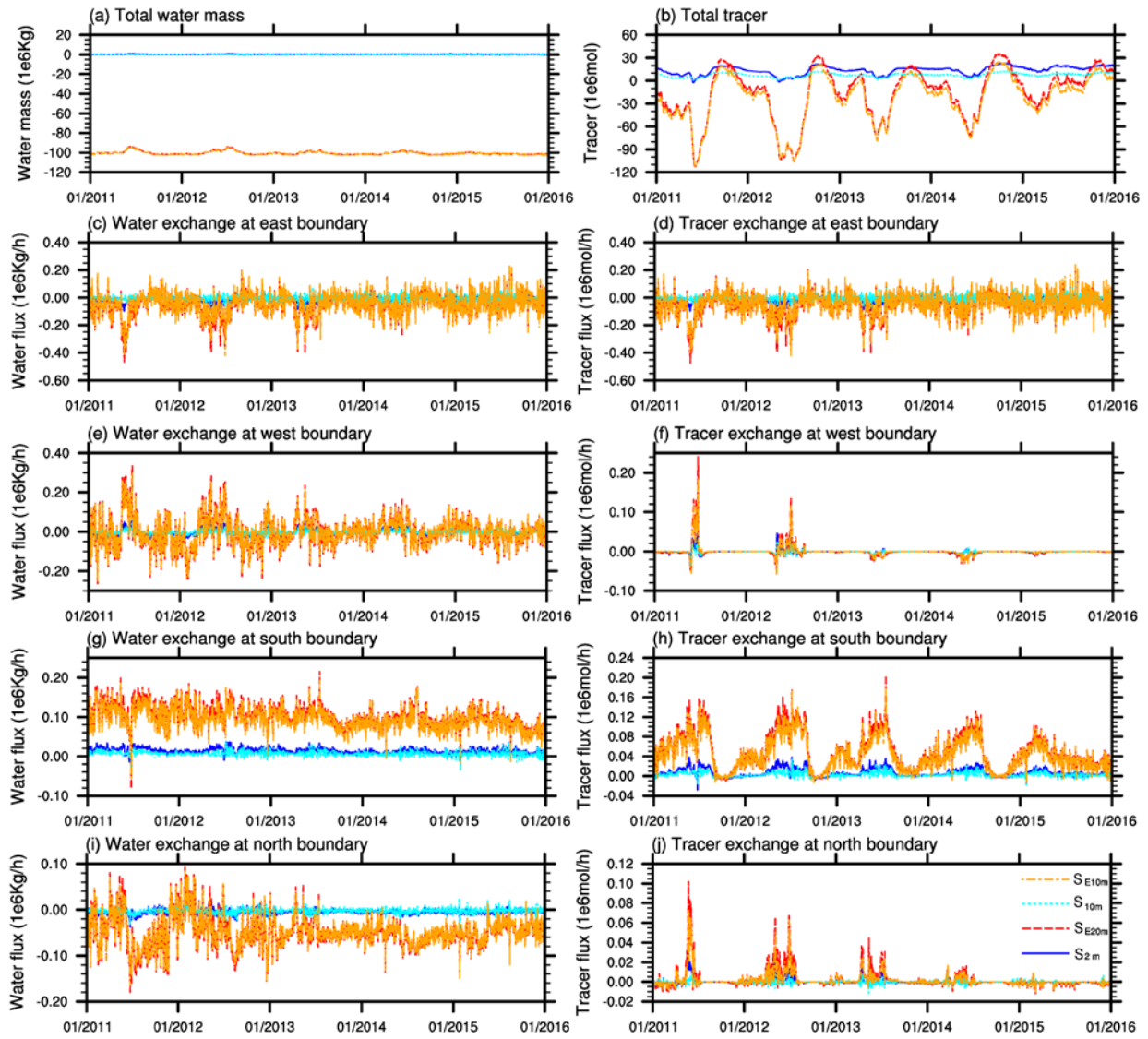
1004  
1005

1006 Figure 11. Liquid saturation levels (unitless) across a transect perpendicular to the river ( $y=200m$ ) on 30  
1007 June of each year in the study period from (a)  $S_{2m}$  and (b)  $S_{E2m}$



1008

1009 Figure 12. Deviations of simulated domain-average latent heat and sensible heat fluxes from those  
 1010 simulated by  $S_{2m}$  (for  $S_{10m}$  and  $S_{20m}$ ), and by  $S_{E2m}$  (for  $S_{E10m}$  and  $S_{E20m}$ ).



1011  
 1012 Figure 13. Deviations of total water mass, tracer, and exchange rates of water and tracer at four boundaries from  
 1013 those simulated by  $S_{2m}$  (for  $S_{10m}$  and  $S_{20m}$ ), and by  $S_{E2m}$  (for  $S_{E10m}$  and  $S_{E20m}$ ).

1014

1015

1016

1017